REVISION 2

The role of magma mixing, identification of mafic magma inputs, and structure of the underlying magmatic system at Mount St. Helens

WILLIAM P. LEEMAN[1]

DIANE R. SMITH[2]

[1] Department of Earth, Environmental, and Planetary Sciences, Rice University, Houston, TX 77251; now at 642 Cumbre Vista, Santa Fe, NM 87501; leeman@rice.edu

[2] Department of Geosciences, Trinity University, San Antonio, TX 78212; dsmith@trinity.edu

ABSTRACT

Mount St. Helens (MSH) volcano, in the southern Washington Cascades arc, has produced dominantly dacitic to andesitic magmatic products over the last 300 ka. Basaltic to basaltic andesitic magmas erupted only during the relatively brief (ca. 2100-1800 yrs. B.P.) Castle Creek period from vents separated by no more than a few kilometers. They provide a unique perspective on the evolution of this volcano. Despite close temporal and spatial proximity, these mafic magmas define two distinct compositional lineages: [A] low-K tholeiites (LKT), and [B] basalts of 'oceanic island' or intraplate affinity (or IPB). Both lack typical arc geochemical signatures and appear to derive from distinct mantle sources, neither of which has been significantly modified by slab-derived fluid or melt components. No true calcalkalic basalts have erupted from MSH despite its obvious arc setting. Each lineage includes derivative lavas that range from ~7 to 5 wt% MgO and ~49 to 55 wt% SiO_2, and both are slightly porphyritic with dominantly olivine and plagioclase, minor spinel, and trace clinopyroxene in some but not all samples. With respect to incompatible elements (e.g., K, La, Nb, Th, etc.), compositional trends for the two lineages are dramatically different and inconsistent with simple fractional crystallization processes. The data instead suggest that each lineage

was produced dominantly by mixing between distinct parental LKT and IPB basaltic magmas and material of intermediate composition roughly similar to average MSH andesite. Mineralogical characteristics of macrocrysts in MSH basalts indicate that they do not represent equilibrium assemblages. Olivine compositions and textures in some samples implicate accumulation of crystals formed from multiple magmas, and evidence for magma mixing is reinforced by the rare presence of 'blebs' of rhyolitic glass. These assemblages of crystals presumably are derived from different magmas and/or older MSH magmatic products (including crystal mush zones) within crustal conduit systems.

Extrapolation of compositional trends ('mixing arrays') to higher MgO content implicates involvement of three types of parental magma: primitive LKT as well as distinct nepheline- and hypersthene-normative IPBs (or ne-IPB and hy-IPB), variants of which have erupted repeatedly from monogenetic vents in this sector of the Cascades. Such magmas are interpreted to form from distinct lherzolitic mantle sources (less fertile, with lower clinopyroxene content for LKT) at depths on the order of 80 (LKT) and 50-60 (IPBs) kilometers, under near-anhydrous conditions, in response to decompression- rather than flux-melting.

We also report a set of self-consistent estimates of temperature, pressure, water content, magma density, and weight fraction of 'andesitic' mixing component for samples of each lineage. These parameters are highly correlated and serve to constrain the structure of the magma feeder system beneath MSH. A dynamic continuum of melt compositions is likely present, controlled principally by temperature and density gradients within the system. We envisage that during Castle Creek time the most primitive basaltic magmas formed distinct reservoirs in the deep crust, with the ne-IPB variant near 28 km depth and the LKT variant near 23 km. More silicic members of these lineages appear to have evolved at depths between ~20-15 km. We suggest that reservoir depths were controlled mainly by magma density that, in turn, is largely determined by the degree of mixing with 'andesitic' components at crustal depths. This configuration implies a vertical magmatic plexus with connections extending well into the upper mantle. The sharp chemical distinction between the LKT and IPB mixing arrays suggests that the respective feeder systems were isolated and rarely interacted despite their close proximity.

2

Finally, it appears that the presence of large, complex, and long-lived conduit systems beneath stratovolcanoes can act as 'magma traps,' within which deeper-seated (mantle) inputs are prone to modification by interaction with stored magmas and their differentiation products. In contrast, the occurrence of relatively primitive basalts from monogenetic vents distal from stratovolcanoes implies that diverse basaltic magmas ascend beneath virtually the entire arc segment, and that the true complexity of this 'mantle wind' is locally masked by modifications within the crust.

Keywords: Cascades arc, Mount St. Helens, basalts, magma mixing, magma plumbing

INTRODUCTION

The modern Cascades volcanic arc is unique among convergent margin settings in that it is associated with an unusually warm subduction zone (Leeman et al., 1990; Harry and Green, 1999; Syracuse et al., 2010). An important consequence is that the downgoing slab undergoes dehydration at relatively shallow depths, with significant loss of aqueous fluids in the frontal arc region (Bostock et al., 2002; Brocher et al., 2003). Thus, fluxes of slab-derived fluids beneath the active volcanic belt are inferred to be among the lowest known (Rondenay et al., 2008; van Keken et al., 2011). This is manifest by almost negligible enrichment of fluid mobile elements like B in Cascades basaltic magmas (Leeman et al., 2004; Manea et al., 2014), and by high estimated magmatic temperatures consistent with their formation under near-anhydrous melting conditions in the underlying mantle (Leeman et al., 2005). Another unique feature is the widespread distribution of essentially contemporaneous but diverse types of primitive magmas in many sectors of the Cascades.

Primitive basalts in southern Washington and northern Oregon (i.e., Cascades Columbia Transect, or CCT; cf. Leeman et al., 1990, 2005; Bacon et al., 1997; Conrey et al., 1997, 2009; Rowe et al., 2009) include the following chemically distinct variants: [a] low-K, high-Al tholeiites (LKT), [b] a spectrum of basaltic magmas of both hypersthene- and nepheline-normative variants, with 'enriched' or OIB-like intra-plate basalt (IPB) trace element distributions, and [c] a spectrum of arc-like calcalkalic basalts (CAB) and basaltic andesites (BA), including some with elevated K_2O ranging to shoshonitic (SHO) compositions. Although the LKTs and IPBs are chemically distinct, primitive variants of

3

both have low Ba/Nb (<20) ratios overlapping with many oceanic basalts, whereas the CAB calcalkalic variants are consistently distinguished by elevated Ba/Nb (>20) ratios that are characteristic of many arc basaltic lavas (Leeman et al., 2005). The proportions of such magmas, and their subtypes, vary spatially along the Cascades arc. For example, LKTs are rare in the northern part of the arc and more common to the south, and may be associated with intra-arc extension (cf. Bacon et al., 1997; Conrey et al., 1997; Green, 2006). Conversely, IPB magmas are less prominent in the southern Cascades (cf. Bacon et al., 1997; Borg et al., 1997; Grove et al., 2002).

Here, we make the case that basaltic magmas erupted from Mount St. Helens (MSH) consist only of the distinctive LKT and IPB varieties. Although it has been proposed that CAB-like basaltic andesites comprise another distinctive magma type at MSH (Clynne et al., 2017; Pallister et al., 2017), we consider these to be products of magma mixing as explained below. We stress the role of basaltic magmas in the framework of overall magmatic activity at MSH. This work bears on the general problem of identifying distinct primitive magmas in settings where magma chemistry may be obscured or modified by complications attending magma ascent and/or storage, including magmatic differentiation and/or hybridization due to mixing with other magmas. This is a critical step in understanding the petrogenetic and tectonic implications of the observed magma diversity.

For example, is magma diversity a manifestation of mantle heterogeneity or a consequence of diverse processes operating on common magma sources and/or the melts derived therefrom? Several papers propose that the observed magma diversity could originate from processes of flux melting, wherein degree of melting correlates with the magnitude of fluid additions to the mantle (Borg et al., 1997; Reiners et al., 2000, Rowe et al., 2009). In contrast, Leeman et al. (2005) propose that distinct mantle sources in a compositionally stratified mantle wedge could generate the different magma types, depending on the depth of melting.

Before addressing such issues further, it is critical to identify magma compositions that are little (or least) modified from primary direct melts of the mantle. Because mixing or mingling of diverse magmas has long been inferred at many arc volcanoes (e.g., Sakuyama, 1981; Streck et al., 2002), locally within the Cascades (Anderson, 1976;

4

Green, 1988; Bacon, 1990; Donnelly-Nolan et al., 1991; Strong and Wolff, 2003; Streck et al., 2007, 2009; Streck and Leeman, 2018), and specifically at Mount St. Helens (Pallister et al., 1992; Smith and Leeman, 1993; Gardner et al., 1995; Mattos, 2006; Lieuallen et al., 2009; Wackett and Smith, 2013), it is reasonable to question whether any magmas satisfy this condition.

MOUNT ST. HELENS BASALTIC ERUPTIONS

Activity at Mount St. Helens (MSH) volcano initiated ~300 ka ago and has continued intermittently to the present (Mullineaux and Crandall, 1981; Clynne et al., 2008; Pallister et al., 2017, provide a current perspective of the eruptive history). Over much of its history, eruptive products have been dominantly dacitic, with subordinate andesite (cf. Smith and Leeman, 1987, 1993; Pallister et al., 1992, Gardner et al., 1995; Clynne at al., 2008). Although basaltic magmas are thought to have played an important role throughout the life of MSH (e.g., as evidenced by relict mafic clots or refractory minerals observed in some MSH andesite-dacite eruptive products; cf. Smith and Leeman, 1987, 1993; Pallister et al., 1992; Heliker, 1995; Carroll et al., 2008; Carroll, 2009; Lieuallen et al., 2009), actual effusion of basaltic lavas was restricted to the Castle Creek eruptive episode that spanned approximately 300 years (between ca. 2100-1800 yrs. B.P.) as constrained by ^{14}C dating and paleomagnetic data (cf. Greeley and Hyde, 1972; Clynne et al., 2004, 2008, 2017). Early Castle Creek products include andesitic to dacitic lavas, domes, and pyroclastic deposits. Beginning ca. 1900 yrs B.P., multiple thin basaltic lavas (mapped as pre-Cave and Cave basalt) and minor pyroclastic deposits erupted from vents on the southern flank of the volcano; these were shortly followed (ca. 1800-1700 yrs. B.P.) by additional basaltic, basaltic andesite, and andesitic products erupted primarily on the northern and northwestern flanks. Collectively, these lavas essentially provide a 'snapshot' of mantle processes during this brief window of time. Here we review compositional, mineralogical, and textural features of representative Castle Creek basaltic lavas. Sampling locations are shown in Figure 1. Note that stratigraphic sequences of several successive lavas were collected in two areas on the north and northeast flanks of the volcano.

5

SAMPLES AND ANALYTICAL METHODS

Samples

We consider here major element data for 36 MSH basaltic to basaltic andesite lavas, as well as trace element and isotopic data for a subset of these samples (Table 1 and Supplement Figure A1). Samples include materials collected from the southern and northwestern flanks of the volcano, as well as the northern flank prior to its partial destruction during the eruption and sector collapse of 18 May 1980. Table 1 also provides data for two MSH low-silica andesites and five primitive CCT basalts (from the nearby Indian Heaven and Battleground volcanic fields, cf. Fig. 1 inset). Data in Table 1 include new and previously published results and the relevant data sources are indicated. In Table 2, we also present new SEM images and analyses of olivine grains occurring in 16 MSH lavas and the 5 primitive basalt samples.

Analytical methods

The data presented in this paper were obtained by multiple methods; precision and accuracy are discussed in the references provided. A JEOL JSM-6010LA SEM/EDS at Trinity University was used to obtain back-scattered electron images and analyses of some 400 olivine grains using polished and carbon-coated thin sections. Operating conditions include 20 KeV accelerating voltage, 10 mm working distance, and 30 second count times. For EDS spot analyses, replicate analyses of NMNH 11131244 (olivine from San Carlos, Arizona) and direct comparison with EMP analyses indicate analytical error of less than ± 1 mol% forsterite in olivine. A JEOL JXA-8200 electron microprobe (Department of Geological Sciences, University of Texas at Austin) was used to confirm spot analyses of selected olivine grains using natural and synthetic mineral standards, 15 KeV accelerating voltage, 30 nA beam current, and 1 μm spot size (cf. Smith and Leeman, 2005). Whole-rock chemical analyses were obtained by methods described previously (cf. Norman et al., 1989; Smith and Leeman, 1993; Johnson et al., 1999; Leeman et al., 2005) as follows: major and some trace elements by XRF either at the University of Edinburgh or Washington State University, and by ICP-OES at Rice University; additional trace element data were obtained by ICP-MS at Washington State University and/or Rice University (cf. Knaack et al., 1994; Horodyskyj et al., 2009). Sr-

6

Nd-Pb isotopic analyses were obtained by TIMS at the Open University (cf. Leeman et al., 1990) and, for some Sr-Pb isotopic analyses, by MC-ICP-MS at the University of Arizona. Analytical data and additional details are provided in Table 1 and Supplement Table A1 (the latter contains all available Sr-Nd-Pb and O isotopic data for MSH eruptive materials). For comparison, average compositions for MSH andesites and dacites, and for primitive end member mafic lava types from the CCT are presented in Supplement Table A2; these analyses were used in numerical models discussed in this paper.

BULK ROCK COMPOSITIONS

MSH mafic lavas range from basalt to basaltic andesite (~49-55 wt% SiO_2), with MgO contents up to 7 wt%. As previously noted, these lavas have been considered to fall into three distinctive groups: low-K and high-K basalts, and basaltic andesites (Smith and Leeman, 1993; Clynne et al., 2017). A principal observation is that the analyzed samples define essentially two distinct and coherent trends on many variation diagrams, particularly those involving incompatible elements (cf. Figs. 2-4; also see additional plots in Supplement Table A3). Based on such diagrams, these samples are discussed here in terms of two groups. **Group A** (all southern flank) lavas include multiple flow units of the Cave basalt, as well as slightly older pre-Cave flows – all of which have similar paleomagnetic orientations (Hagstrum et al., 2002; M.A. Clynne, 2003, personal communication). Cave basalt lavas issued from a vent area (now buried by younger deposits) on the southwestern flank of MSH at an elevation near 5000' (Williams et al., 2004). Vents for pre-Cave lavas are not well known and some may originate from sources closer to the pre-1980 summit. Collectively, MgO-rich variants of these lavas have systematically lower K_2O and higher CaO and define tight arrays in most variation diagrams; all Group A lavas are distinguishable from Group B lavas by their distinctively higher CaO contents. Incompatible element (e.g., K_2O, P_2O_5, La, Zr, Th, Ta) contents in Group A lavas increase with increasing SiO_2, or with decreasing MgO (cf. Figs. 2 and 3).

Group B lavas are mostly from the northern flank and originated from higher elevation vents located around the pre-1980 MSH summit. These lavas also define coherent trends, but with *opposite* slopes compared to trends for Group A. Their incompatible element contents generally *decrease* with increasing SiO_2 or with

7

decreasing MgO. In detail, Group B lavas from different sampling localities can be distinguished based on composition. For example, a stratigraphic sequence of lavas from the northeast flank of the volcano (DS-4 through DS-9; loc. *Nfa* on Fig. 1) displays generally upward increasing Mg# (= molar Mg/[Mg + Fe], here calculated assuming $Fe^{2+}/\sum Fe$ = 0.85; see Supplement Note 5), consistent with progressively less evolved magmas feeding this package of lavas. Included in this group is the one basalt (SHH-17) described by Halliday et al (1983), albeit it was sampled at a separate location higher on the volcano. These samples are distinctive as discussed below, and designated as subtype B1.

A set of lavas (samples DS-74 through DS-78) from the northern flank (loc. *Nfb*, Fig. 1) is compositionally distinct from the aforementioned sequence, but flows at this site also exhibit an upward increase in Mg#, consistent with eruption of generally less evolved magma over time. Our one sample (L01-17) from the northwestern flank of the volcano is compositionally similar to the *Nfb* lavas, and is lumped with them for purposes of discussion as Group B2-north. A few Group B lavas occur on the southern flank of the volcano; these define coherent compositional trends that are generally similar to *Nfb* samples, but for clarity they are designated as Group B2-south.

Overall, the data are best considered in terms of multiple compositionally distinct basaltic magma inputs. In a plot of FeO*/MgO versus SiO_2 (Fig. 4), the most primitive basalts of each series (<52 wt% SiO_2) have elevated FeO*/MgO and lie within the tholeiitic (TH) field of Miyashiro (1974), whereas more evolved lavas (including MSH andesites and dacites) are calcalkalic in this framework. FeO*/MgO ratios and Mg#s, for the two groups overlap. On the other hand, elevated K_2O (and TiO_2) of Group B1 primitive basalts give them an alkalic character, and some are nepheline-normative.

Trace element compositions of all Castle Creek basaltic lavas are atypical of arc basalts in that they show little or no systematic depletion of high field-strength elements (Nb, Ta, Ti) relative to other incompatible elements, and primitive mantle normalized profiles are similar to those of many ocean island and other intraplate basalts (cf. Leeman et al., 1990; Smith and Leeman, 2005; Fig. 5). However, for the most magnesian (≥ 7 wt% MgO) samples, Group B lavas are enriched relative to Group A by up to three-fold for P_2O_5, K_2O, Rb, Ba, Nb, Ta, La, and Th; and by lesser extents for Sr, TiO_2, Zr, and Hf.

8

Contents of Y, Yb, CaO, Na_2O, Al_2O_3, and most transition metals (V, Sc, Cr, Ni, Mn) partly overlap for the two groups. For most trace elements, MSH Group A and B lavas overlap in composition with regional LKT and IPB lavas, respectively, but are more enriched in alkali elements Cs and Rb (Fig. 5).

Sr-Nd-Pb isotopic compositions of Group A and Group B lavas are similar (Supplement Table A1 and Figure A1). In detail, $^{87}Sr/^{86}Sr$ isotopic ratios are slightly higher in primitive Group A lavas (~0.70313 vs. 0.70300), but increase slightly (to ~0.7033) in both groups with decreasing MgO and grade into more radiogenic compositions of MSH andesites and dacites. $^{143}Nd/^{144}Nd$ isotopic compositions have been measured mainly in higher MgO samples, and are similar (~0.5130) for both groups; these data also grade into slightly less radiogenic compositions of MSH andesites and dacites. Oxygen isotopic compositions of MSH basaltic lavas (whole-rock $\delta^{18}O$ = 5.5 to 6.0 permil) are in the range for typical mantle-derived magmas (Eiler, 2001), and grade to values near 7.5 permil in the dacites. Pb isotopic ratios are somewhat more variable, but overlap for the two groups and show no systematic variation with MgO content except that they also lie on a continuum with more evolved and less radiogenic MSH andesites and dacites.

PETROGRAPHY AND MINERAL CHEMISTRY

Overview

Basaltic lavas of both groups A and B are similar in that they carry phenocrysts of plagioclase, olivine and, in some cases, trace clinopyroxene along with minor spinel inclusions in olivine. Groundmasses largely comprise plagioclase, olivine, clinopyroxene and aphanitic to glassy interstitial material. Plagioclase phenocryst populations (typically <10-15 vol%) are diverse and commonly include many grains (especially in Group B and some pre-Cave Group A basalts) that appear to have had complex histories (oscillatory zoning, resorption, sieve-like zones, etc.) indicative of mingling or mixing of multiple magmas. Likewise, olivine phenocrysts (≤6 vol%) range from euhedral or skeletal grains with thin normally zoned rims to subrounded or corroded grains, some of which exhibit reversely-zoned rims or thin overgrowths of orthopyroxene. The latter clearly reflect

disequilibrium with the host carrier liquid. To evaluate the significance of these textural relations, representative mafic lavas were investigated by SEM and EMP methods.

Mineral compositions and textures

Available analyses indicate that cores of plagioclase phenocrysts in individual lavas of both group A and B types generally range in composition from An_{70} to An_{80}, with some outliers, and groundmass microlites are generally more sodic (Lewis, 2004; Mattos, 2006). Notably, some MSH basaltic lavas contain reversely-zoned plagioclases with more sodic cores (see below). These data support petrographic inference that the feldspars comprise a complex assembly in MSH lavas (also cf. Streck, 2008; Streck et al., 2008), and they are utilized later in this paper to evaluate magmatic temperatures and water contents.

A major focus of the present paper is on the olivine populations of MSH lavas. Detailed compositional data and backscattered electron (BSE) images were obtained for representative olivine grains in 14 Castle Creek age mafic lavas, one Kalama age (ca. 1500 C.E.) andesite, and five Quaternary age primitive basaltic lavas (MgO ≥ 8 wt%) representing compositional variants in the region proximal to MSH. Nearly all grains exhibit normal zoning to more Fe-rich compositions in thin zones at the rims. However, the core compositions often reveal more complicated histories, and these are described below. Our data are summarized in Table 2. We include microprobe data for the NW flank lava (L01-17; Lewis, 2004) and note that maximum-Fo core compositions are virtually identical to analyses (Fo_{83} vs. Fo_{84}) of the same sample analyzed by Carroll (2009). Likewise, Carroll's maximum core compositions for sample PB-28 are very similar to results reported in Table 2 (Fo_{83} vs. Fo_{86}). Size-composition relations for olivine phenocryst *cores* are also portrayed in Figure 6.

The first order observation is that most MSH samples exhibit significant variability in olivine core compositions, with ranges as follows (Table 2): Group A, Fo_{86-71}; Group B, Fo_{85-58}. To avoid specific genetic implications (i.e., whether they are phenocrysts, antecrysts, or xenocrysts), we refer to relatively large euhedral to blocky grains with apparently uniform core compositions as "macrocrysts." In some samples, core Fo contents generally decrease with grain size, akin to 'normal' zoning as commonly

observed in individual olivine grains; this pattern is referred to here as 'normal'. Such patterns are observed in MSH samples DS-27 (Fig. 6A), DS-9 (Fig. 6C), and several primitive CCT basalts (Fig. 6D). In contrast, other samples show either no clear correlation between composition and size (e.g., DS-30, DS-32), or a rise in Fo content with decreasing size (e.g., DS-71, DS-74, DS-77). These abnormal patterns are characteristic of many Group B2 lavas.

Table 2 lists calculated forsterite contents of olivines in equilibrium with liquids having Mg#s of MSH bulk rock samples. Again, as inferred for many Cascades mafic lavas (cf. Smith and Leeman, 2005; Leeman et al., 2005; Rowe et al., 2009), it is assumed that the mole fraction of ferrous iron in the whole rock is 0.85, as expected for magmas slightly more oxidized than the quartz-fayalite-magnetite (QFM) redox buffer. The Fe/Mg distribution coefficient (K_D) is assumed to be 0.3 (cf. Roeder and Emslie, 1970), which is consistent with such redox conditions. In few cases, maximum olivine core forsterite content is greater than the predicted equilibrium composition. More typically, cores of olivine macrocrysts in most samples range to much lower Mg# than predicted for equilibrium with liquids similar to the bulk rock compositions.

Such relations are conveniently visualized in so-called Rhodes diagrams (cf. Rhodes and Dungan, 1979), where olivine compositions are plotted as mol% Fo versus the whole-rock Mg#, and the data compared with idealized loci of equilibrium compositions. Figure 7 illustrates how this diagram can be used to rationalize compositions of olivine cores in the Kalama andesite (DS-79). Assuming the bulk rock composition (Mg# ~54) is representative of the actual carrier magma, the expected equilibrium olivine should have a composition near Fo_{80}. One can infer that [1] olivines more Fo-rich than the locus of equilibrium compositions must have formed from liquids with a higher Mg# than the host magma, and [2] olivines less Fo-rich than the locus of equilibrium compositions must have formed from liquids with a lower Mg# than the host magma. The andesite carries some olivines (~Fo_{81-79}) that could have formed from a liquid of its bulk composition, but most olivines in this sample presumably formed from lower Mg# liquids (e.g., ~40 for Fo_{70} olivine and ~33 for Fo_{60}). This sample also carries olivines that are more Fo-rich (up to Fo_{83}) than the equilibrium composition; these grains could have been inherited from liquids of higher Mg# (up to ~60). BSE images of representative

11

olivine grains (insets in Fig. 7) show that resorption and reaction textures are evident, particularly on smaller and lower-Fo grains. Such diagrams are presented here primarily to emphasize the diversity of olivine cores and corresponding textural relations within individual samples.

Figure 8 shows olivine data for Group A lavas. Olivine grains in these rocks tend to be subhedral to euhedral with nearly uniform cores and thin normally zoned rims. Samples PB-30 and PB-32 exhibit maximum-Fo olivine cores ($\sim Fo_{82-79}$) near equilibrium values for the bulk rock Mg#. Considering that PB-32 and DS-27 (with maximum Fo of 82 and 77, respectively) are found in close proximity (locations 1 and 2; cf. Fig. 1), the difference in their olivine compositions is likely due to sampling bias among the analyzed grains in each sample. Independent microprobe analyses of PB-32 olivines reveal core compositions at least as magnesian as Fo_{78} (Carroll, 2009). Minimum-Fo olivine cores (Fo_{73-71}) could have formed from more Fe-rich liquids (Mg# = 43-47).

Figures 9 and 10 show Rhodes diagrams for Group B lavas. Several samples have Fo-rich olivine cores consistent with inheritance from higher-Mg# liquids. Most have a continuum of olivine core compositions ranging down to Fo_{78-70} for *Nfa* samples and as low as Fo_{64-58} in some *Nfb* samples. In general, the lower Fo grains exhibit textural evidence of disequilibrium (e.g., partial resorption) and, in some cases, reverse zoning (e.g., sample DS-72, Fig. 9).

Among Group B lavas, of particular note are samples DS-4 (subgroup *Nfa*) and DS-74 (subgroup *Nfb*). Both samples exhibit strong textural and mineralogical evidence of magma mingling/mixing processes, as seen in photomicrographs of these samples (Figs. 11, 12). DS-4 is a relatively high-MgO basalt (Mg# = 60.6). This lava has a distinctive texture with what appear to be dark glassy globules (up to cm-scale) surrounded by intersertal to holocrystalline matrix (Fig. 11A-11B). The globules contain grains of equant olivine and plagioclase, very few of which exhibit obvious disequilibrium textures. However, core compositions are variable for both olivine (Fo_{85-83} with outliers as low as Fo_{78}) and plagioclase (An_{71-64}, with an outlier of An_{49}). The intersertal matrix carries a variety of olivine and plagioclase grains, many of which exhibit rounding or partial resorption and sieve-like interiors. For example, one plagioclase with a sieved mid-interior is reversely zoned with a core of An_{61} and rim of An_{77}. Olivine core

12

compositions in the matrix are varied and overlap the range of olivine core compositions (Fo_{87-77}) occurring in the globules. Also present in this lava is a brown glassy 'bleb' (Fig. 11C) containing microphenocrysts of orthopyroxene grains (Mg# ~64-65), small patches of brown, silicic (~74 wt% SiO_2) glass, and plagioclase with core compositions of An_{60-58}. This material is considered to be "cargo" or a relict of evolved magma that inefficiently mixed with the host basaltic magma.

DS-74 is a relatively evolved basaltic andesite (Mg# = 52.0). Olivine cores exhibit a large range in composition, from Fo_{81} to Fo_{58} (Figs. 9 and 12). Olivine textures range from euhedral to embayed and/or partly resorbed with decreasing grain size (~500 to 50 μm; Figs. 6, 12). Larger euhedral to equant grains have maximum-Fo cores (Fo_{81-79}), with iron enrichment at their rims (to Fo_{66-61}; Fig. 12A-C). Smaller (~250 μm) grains have less magnesian cores (Fo_{76-70}), iron enrichment at their rims (to Fo_{65-61}), and orthopyroxene reaction rims (Fig. 12D-F). Grains less than 100 μm in size are distinctly less magnesian (down to Fo_{57}), strongly embayed, and surrounded and partly invaded by orthopyroxene overgrowths (Mg# = 64-66; Fig. 12G-H). These observations suggest that larger grains have reacted with liquids more Fe-rich than equilibrium magma(s), and that the degree of reaction increased with decreasing grain size. The smallest olivine grains with core compositions of Fo_{63-58} are far from equilibrium with the host carrier liquid, supporting an antecrystic or xenocrystic origin for these grains.

For comparison, representative CCT primitive basalts (Supplement Figure A2, in Supplement Note 2) carry olivine populations in which maximum-Fo is close or equal to calculated equilibrium compositions. Notably, bulk Mg# and equilibrium Fo increase from LKT to IPB to SHO basalts. Nevertheless, all samples examined carry olivine macrocrysts ranging to at least 8 mol% Fo below expected equilibrium values. Unlike MSH lavas, olivine grains in these primitive basalts do not display obvious disequilibrium textures.

To summarize, the petrographic and mineral composition information for MSH basaltic lavas provide compelling evidence for open system evolution of these magmas involving mixing and mingling between multiple distinct liquids. Diversity of the olivine core populations is particularly notable, and not readily explicable in terms of progressive fractionation of a specific magma. Moderate ranges in composition of olivine

13

macrocrysts are observed in mafic lavas from many geologic settings, and are variously ascribed to: [1] entrainment and disaggregation of cumulate material or mafic to ultramafic wall rocks (Garcia, 1996; Maclennan et al., 2003; Thomson and Maclennan; 2013); [2] acquisition of crystal cargo due to interaction with magmatic crystal mush zones (Zellmer et al., 2016); [3] magma mixing (Rhodes and Dungan, 1979; Reubi et al., 2002; Maclennan et al., 2003); and/or [4] crystal fractionation processes (Maclennan et al., 2003). At MSH, it is likely that olivine macrocryst populations in a given lava represent mixtures of [1] near-equilibrium crystals (true phenocrysts), in some cases [2] crystals inherited from slightly more primitive liquids than the host, and in most cases [3] an assortment of crystals derived from more evolved liquids or crystal "mushes" within the overall magma conduit system. The first two variants typically exhibit normally-zoned rims, whereas the latter display the strongest textural evidence of disequilibrium and attempted re-equilibration with the host liquid (embayments, orthopyroxene overgrowths and/or reverse zoning). The range in macrocryst core compositions attests to the complexity of magma interactions beneath MSH. Moreover, preservation of the observed disequilibria features in samples DS-4 and DS-74 is consistent with the occurrence of magma mixing events shortly (no more than days to months?) prior to eruption of these lavas (cf. Costa et al., 2013; Beier et al., 2017; Oeser et al., 2018).

DISCUSSION

As previously noted (Smith and Leeman, 1987; Pallister et al., 1992, 2008), trace element chemistry of MSH evolved lavas precludes their derivation from the associated basaltic lavas by normal fractional crystallization processes. In particular, the least-evolved dacites (~2 wt% MgO) have contents of Ta, Zr, and LREE overlapping those of Group A basalts, and in most cases *lower* than those of most Group B basalts. This is clearly illustrated in an enlarged plot of MgO vs. K_2O (Fig. 13) in which MSH mafic lavas define three distinct near-linear trends: M1, for all Group A lavas; M2, defined mainly by ne-normative lavas from location *Nfa*; and M3, for hy-normative Group B lavas from locations *Nfb*, *Nfc* and the south flank. Similar relations can be seen for virtually all incompatible elements (Ti and P in Fig. 2; La, Zr, Th, and Ta in Fig. 3; Ba and Nb in Supplement Table A3). These trends intersect at low MgO content (between

14

4-5 wt%) near the composition of average Castle Creek andesite, and they project toward average compositions of three distinct regional basalt types as previously noted (i.e., near 8 wt% MgO). Superimposed on this diagram are representative fractional crystallization (FC) curves originating at the average composition of ne-normative IPB (ne-IPB) and low-K tholeiite (LKT). For the LKT end member, two curves are shown that simulate combined olivine and plagioclase removal assuming different proportions of these phases (FC1a, ol:plag = 0.3:0.7; FC1b, ol:plag = 0.9:0.1). For the ne-IPB end member, one curve is shown (FC2, ol:plag = 0.3:0.7). Details of these calculations are presented in Supplement Note 3 and Table A3.

The relevant point is that fractional crystallization, by itself, cannot replicate the observed compositional trends for MSH mafic lavas. For LKT-like magmas (Group A lavas; trend M1), K_2O increases with decreasing MgO, but more rapidly than predicted by any realistic fractional crystallization process. Conversely, for ne-IPB parental magmas (Group B1; trend M2), K_2O *decreases* with decreasing MgO, whereas fractional crystallization processes would result in an *increase*. This latter result is the case for all strongly incompatible elements (Rb, Th, Ba, Nb, etc.; cf. Supplement Table A3). We also note that strongly compatible elements such as Ni or Cr behave similarly in Group A and B lavas but are depleted more rapidly by realistic fractional crystallization processes than actually observed (cf. Supplement Table A3). The behavior of these elements could reflect some dilution in response to mixing with, or assimilation of, evolved melt components. Finally, an intermediate array can be discerned in Figure 13 for which K_2O contents are near constant as MgO decreases; these are the Group B2 lavas. Some of these straddle a tie-line (M3) between average hy-IPB primitive basalt and average MSH andesite. There appears to be some overlap in Figure 13 for Group A and Group B samples with less than 6 wt% MgO, but the two subsets are readily distinguished with respect to CaO contents (>9 wt% vs. <8 wt%, respectively; cf. Fig. 2).

Mixing scenarios

MgO-variation diagrams for major oxides (Fig. 2) show that arrays for Group A and B lavas lie between primitive CCT basalts and converge near 5 wt% MgO, indicating that the primitive basalts could have interacted or mixed with andesitic magma(s) (or similar

15

composition material) within the MSH feeder system to produce those arrays. We evaluate the observed near-linear arrays (M1, M2, and M3) in terms of mixing between three different varieties of basaltic magma (approximated as average LKT, ne-IPB, and hy-IPB, respectively) and more silicic magma similar to average MSH andesite (see Supplement Table A2 for end member compositions). Scatter in observed MSH compositions relative to the mixing arrays can be attributed to subtle differences in compositions of the selected mixing end members, and/or minor analytical uncertainties. Also, it is likely that there are secondary contributions from fractional crystallization processes, as seems particularly evident for lavas (from location *Nfa*) along the M2 array.

Assuming that mixing is the dominant control over compositions of erupted MSH basaltic magmas, we have estimated linear mixing proportions for samples distributed along trends M1, M2, and M3. This was accomplished using a major element least-squares mixing model, the average end member compositions noted above, and the Solver tool in Excel (cf. Streck and Leeman, 2018). Detailed results are presented in Supplement Note 4 and Table A4. For example, we show that there appears to be a near-linear relation between lava composition (e.g., MgO content) and the proportion of 'andesitic' material admixed with the respective postulated primitive basalt end members. Estimated mixing proportions based on major elements were used to independently simulate the trace element compositions of the analyzed lavas. As shown in Supplement Note 4 and Figure A3, the ratio of calculated vs. observed concentrations for selected trace elements in representative samples generally agree within expected uncertainties (on the order of ± 20%). Lastly, available Sr isotopic compositions can be reasonably reproduced by the proposed mixing scenarios, provided that the basaltic inputs have $^{87}Sr/^{86}Sr$ ratios near 0.7030 (cf. Supplement Table A4 for details and plots).

Based on these results, we conclude that mixing processes reasonably explain much of the compositional variation observed in MSH mafic lavas, albeit there is leeway in the specific magmatic end members we have considered, and use of specific andesitic compositions (instead of the average) might more precisely reproduce the mixing arrays. Other processes, such as fractional crystallization, clearly fail to explain the observed compositional variations. We cannot exclude the possibility of some form of wall rock assimilation, but the petrographic evidence strongly implicates contributions from

16

relatively evolved magmas. We note that contents of CaO in Group A lavas are difficult to reconcile with a dominant mixing model, in which case involvement of a more calcic assimilant is required. However, the persistence of elevated CaO in the more evolved lavas of Group A can be reconciled with combined mixing and fractional crystallization if olivine:plagioclase proportions are intermediate (ca. 1:1) to values used in the two models in Supplement Table A3.

Mantle inputs to the MSH magmatic system

Primitive basalts elsewhere in the CCT provide additional insights into the nature of mantle inputs beneath MSH. Regional LKTs (from the frontal arc Portland Basin and nearby Indian Heaven and Mount Adams volcanic fields) have MgO ranging up to nearly 10 wt% and lie along projections of MSH Group A basalts to which they may be considered parental (Figs. 2-3). In contrast, there is considerable variance among primitive IPB compositions. For these lavas, median MgO is near 8 wt%, and ne-normative variants contain up to ~1.6 wt% K_2O; many of these magmas lie along projections of the MSH Group B basalt arrays and could be considered as reasonable parental liquids to such magmas. In Figure 13, we also show a hypothetical mixing vector between average LKT and average ne-IPB. From this perspective, data for some hy-IPB lavas might be attributed to mixing between primitive LKT and ne-IPB magmas. However, because mixing proportions vary widely depending on which elements are considered, we conclude that average hy-IPB cannot be a product of mixing these specific end members. For similar reasons (see Figs. 2 and 3), we also consider that significant local mixing between Group A and Group B lavas at MSH is unlikely.

Compositional distinctions among the regional primitive basaltic magmas could reflect heterogeneities in source compositions and/or variations in melting conditions (e.g., degree of melting) as discussed in Supplement Note 6 (cf. Fig. A4) and Note 7. For example, differences in CaO content between LKT and other IPB primitive basalts can be attributed to derivation of primitive LKT parental liquids from a relatively clinopyroxene-poor source (e.g., spinel lherzolite). These ideas will be discussed in more detail in a separate paper.

17

Magma formation conditions

To better understand conditions of formation for the respective magma types, it is necessary to reconstruct compositions of their precursor magmas. Rather than attempt to unravel the documented complexities of erupted MSH lavas, we start with the assumed primitive mixing end members themselves. As proxies for purposes of this paper, we specifically model primitive CCT magma types represented by lava samples listed at the bottom of Table 1. These samples are all phenocryst-poor ($<\sim$5-10% total), with only olivine in the IPBs and olivine plus plagioclase in the LKT. Each bulk rock analysis was adjusted by incremental addition of equilibrium olivine to approximate the composition of a primitive magma in equilibrium with olivine of Fo_{90} (i.e., source with Mg# = 90; see Supplement Note 7 and Table A6; cf. Leeman et al., 2005). Because actual source compositions are unknown, similar calculations were also made for more refractory sources (Mg#s 91, 92). It is assumed that all primitive magmas had peridotitic sources with molar X-fe3 = 0.15 (cf. Smith and Leeman, 2005, Lee et al., 2010). Equilibration with an assumed Mg#90 source requires addition of 21.4% olivine to the LKT, and about 13% olivine to the various IPBs. Physical conditions at which such primitive liquids could have last equilibrated with their mantle source have been estimated using several thermobarometers that yield comparable results (cf. Leeman et al., 2005; Lee et al., 2009; Plank and Forsyth, 2016; and references therein). Adopting estimates from the Lee et al. (2009) algorithm, values for temperature, pressure, and depth are greater for the LKT (1460°C, 2.4 GPa, ~80 km) than for the three IPB liquids (near 1370°C, 1.5-1.75 GPa, ~50-60 km) for equilibration with a Mg#90 source. These can be considered as 'minimal' P and T conditions for melt segregation from the mantle. For more refractory (higher Mg#) sources, these parameters will be commensurately higher (cf. Supplement Table A6). However, for segregation conditions to converge for LKT and IPB primitive mantle melts, source Mg# for the IPBs would have to be substantially higher (e.g., 91.5 vs. 90). Notably, all of these calculated loci of melt equilibration lie slightly above the dry solidus for peridotitic mantle (Hirschmann, 2000; Leeman et al., 2005; cf. Supplement Table A6, cell K48). The effect of water on calculated temperatures is a reduction of approximately 30°C per wt% H_2O (Leeman et al., 2005; Médard and Grove, 2008; Plank and Forsyth, 2016). But because the Cascades is a 'hot, dry' arc, it is

18

expected that magmatic water contents will be low, and this is borne out by measurements of H_2O in Cascades basaltic melt inclusions (cf. Sisson and Layne, 2000; Le Voyer et al., 2010; Rea et al., 2012). This view is supported by estimates of magmatic water contents at MSH, as discussed below.

While absolute depths of magma segregation may have uncertainties of at least several km, it appears that primitive LKT magmas are likely to derive from relatively greater depths and warmer mantle domains than the IPB magmas. This is characteristic of the entire CCT transect from backarc to frontal arc (Leeman et al., 2005; Leeman, unpublished data). A plausible explanation is that LKT magmas form by decompression melting within ascending asthenospheric mantle, analogous to the 'hot fingers' concept of Tamura et al. (2002), and supported by thermal modeling of Rees Jones et al. (2018). In the case of the CCT, such mantle upwelling could be focused by extensional deformation associated with oblique subduction along this sector of the Cascades (Wells et al., 2017, and references therein). Moreover, advective heat introduced by ascending LKT magmas could elevate mantle temperatures (cf. Rees Jones et al., 2018) and instigate partial melting of shallower domains, thereby producing the IPB (and possibly other) magmas. As noted by Leeman et al. (2005), calcalkalic magmas in the CCT appear to segregate from even shallower depths, and from more refractory (Mg# >90) sources presumed to lie within non-convective domains in the upper mantle wedge. This is exemplified by olivine-addition calculations for the SHO lava (DS-42-81; cf. Supplement Table A6) and the high Fo content of its olivines (cf. Supplement Fig. A2).

Constraints regarding the MSH plumbing system

MSH basaltic magmas clearly have undergone cooling during their ascent, as attested by their primary phenocryst assemblages. To evaluate physical conditions just prior to eruption, we have determined magmatic temperatures and pressures for each sample using a variety of geothermometers and geobarometers (detailed results are presented in Supplement Note 5 and Table A5). These estimates ideally provide constraints on the structure of the underlying magmatic conduit system. The algorithms utilize major element compositions of the lavas and the extant olivine and plagioclase phenocrysts. As noted above, we apportion FeO and Fe_2O_3 assuming X-fe3 = 0.15; based on this value,

calculated olivine compositions are similar to the most forsteritic olivines in each lava. Temperatures were calculated using so-called 'liquid', 'olivine-liquid,' and 'plagioclase-liquid' thermometers discussed in Sugawara (2000), Leeman et al. (2005), Putirka (2008), and Lee et al. (2009). These results are generally consistent (well within the expected precision of each method) and give temperature ranges of 1203-1148°C for Group A and 1216-1112°C for Group B lavas, in each case decreasing with increasing SiO_2 (Figure 14). Temperatures are considerably more uniform for the least evolved lavas of Group A (Cave basalt; avg. 1192 ± 7°C; N = 15) and Group B1 (*Nfa* location; avg. 1205 ± 7°C; N = 5). Average temperatures for all MSH samples based on olivine thermometers of Lee et al. (2009), Sugawara (2000), and five other thermometers discussed in Putirka (2008) closely agree with an average standard deviation of 11°C. The Lee et al. (2009) temperatures agree with those averages within better than 10°C (with mean Δ = 1°C). Nominal pressures were estimated using the approaches of Lee et al. (2009) and Putirka (2005, 2016); values are in agreement within 0.16 GPa (~5 km depth) on average. However, the Lee et al. thermobarometer most faithfully reproduces test data pressures derived from high P-T experiments (Supplement Table A5, cell L141), and is also favored because pressure is computed independent of a temperature variable. Thus, Lee et al. temperatures and pressures were used as inputs to other algorithms that are pressure- and/or temperature-dependent.

Magmatic water contents were estimated using the plagioclase-melt hygrometers of Putirka (2005) and Waters and Lange (2015), which have nominal uncertainties of 1.0 wt% and 0.35 wt% H_2O, respectively. Both of these methods require as inputs magmatic temperature and pressure estimates as well as compositions of equilibrium plagioclase. For feldspar composition, we used [1] core compositions of dominant phenocrysts in the few samples that have been studied in detail (Lewis, 2004; Mattos, 2006; our unpublished data), [2] a range of more sodic compositions, and [3] an 'optimal' composition (obtained as discussed in Supplement Note 5, and Table A5) that produced the results discussed below. The 'optimal' X_{An} value, in essence, is the plagioclase composition for which the Putirka (2008; eqn. 25a) plagioclase barometry pressure is equivalent to the Lee et al. (2009) pressure for a given sample; 'optimal' X_{An} values are skewed to the sodic side of feldspar composition ranges in MSH lavas. Effects of uncertainties in the input

20

parameters are evaluated in Supplement Note 5 and Table A5 (cell C120). *Relative* differences in estimated water content amount to <3% per mol% An, about 23% per GPa, and <2% per °C. Thus, uncertainty of ± 10 mol% An on the 'equilibrium' plagioclase composition (similar to the observed range in typical MSH basalts) translates to a range of ± 0.3 wt% H_2O for a magma with estimated water content of 1.0 wt%. This is comparable to the nominal uncertainty of the hygrometer, and such uncertainties will not compromise any interpretations in this paper.

Initial Lee et al. (2009) temperature and pressure estimates were input into the Waters and Lange (2015) hygrometer to arrive at preliminary estimates of water content. These water estimates were then iteratively included in the individual lava compositions, and T, P, and water contents were recalculated. After three iterations, values for plagioclase-based T, P, and H_2O content stabilized (cf. Supplement Table A5). Final estimates of water content using the Putirka (2005) and Waters and Lange (2015) hygrometers agree within better than ± 0.5 wt% for all samples, excluding two andesites. For discussion, we use estimates by the latter method. The general outcome (Figure 14 and Supplement Table A5) is that predicted water contents are in the range of 0.2-0.9 wt% (average = 0.59 ± 0.23; N = 15) for most Group A lavas, negligible for most Group B1 (*Nfa*) lavas, variable (0.2-2.2 wt%) for Group B2 lavas, 1.5-1.7 wt% for MSH low silica andesites, and negligible for average primitive LKT (sample DS-80A-80, Supplement Table A5). For comparison, direct analyses of olivine-hosted melt inclusions in two MSH basaltic tephras produced maximum water contents of ~2.2 wt% (Rea et al., 2012, and personal communication). Our result for *primitive* LKT is consistent with derivation of such magmas from a water-poor source. No estimates were made for other primitive CCT lavas owing to absence of plagioclase phenocrysts. Finally, we note that all MSH magmas considered here are strongly water-undersaturated, as predicted solubilities are at least 6 wt% H_2O (at 1150°C, 0.5 GPa; Newman and Lowenstern, 2002) and would further exceed the estimated water contents at magmatic conditions estimated here.

Implications for the magmatic plumbing and transport system

We conclude that basaltic magmas ascended beneath MSH from upper mantle depths of at least 60-80 km, with LKTs derived from deeper and compositionally distinct (less

21

fertile) domains relative to coeval IPBs. It is unclear how the feeder conduits preserve their individual integrity, but we see no compelling evidence that the respective Group A and B magma streams intermingled during Castle Creek time, despite the close proximity of the vents (within a few km of each other) and close timing of the eruptions. We surmise that the respective magma types must have stagnated at lower-crustal depths where they experienced cooling and formed primary olivine and plagioclase phenocrysts. Figure 14 summarizes the calculated depths (pressures), temperatures, H_2O contents, densities, and proportion of the assumed andesite mixing end member for MSH basalts and low silica andesites. Taken at face value (cf. Supplement Table A5, cell L120), pressure estimates (0.70 ± 0.04 GPa; N = 15) for the majority of Group A lavas are coherent and suggest that these magmas stagnated at a depth of 23.0 ± 1.2 km, where they cooled and interacted with pre-existing felsic magmas or intrusive equivalents. The most evolved Group A lava (pre-Cave basalt) gives a slightly lower pressure (0.53 GPa; 17 km). If primitive LKT magmas parental to Group A lavas are nearly anhydrous, then the water contents inferred for Group A lavas are presumably established during deep crustal residence. Pressure estimates for Group B1 lavas are systematically higher (0.86 $\pm$ 0.05 GPa; N = 5, excluding DS-4) and imply that they likely stagnated at greater depth (28.3 $\pm$ 1.6 km) than Group A magmas. Pressure estimates for Group B2 lavas are lower, less uniform, and appear to correlate with bulk composition. Samples with 51-53 wt% SiO_2 give coherent pressure estimates (0.63 ± 0.06 GPa, or 20.7 ± 1.8 km depth; N = 7), whereas those with >53 wt% SiO_2 give systematically lower pressures (0.45 ± 0.05 GPa, or 14.7 ± 1.5 km depth; N = 6). These results are remarkable in that they imply systematic differences in the depths of stagnation for compositionally distinct magma batches. It is important to note that absolute values for pressure (depth) are subject to larger uncertainty than standard deviations on the averages (cf. Supplement Table A5), but we believe that the relative depths are robust and consistent with available geologic constraints.

Figure 15 schematically displays the distribution of magma plumbing beneath MSH in accordance with the inferred pressure estimates. For regional context, the left panel shows estimated segregation P-T relations for primitive CCT lavas (MgO >8 wt%) projected onto a cross-section of the Cascadia subduction zone (cf. Leeman et al., 2005).

22

Pressure/depth calculations, as described in Supplement Note 7 and Table A6, were applied to data from Leeman et al. (2005) and Evarts et al. (2017); in this case, all samples are corrected by olivine addition to Mg# appropriate for source Mg# = 90. LKT lavas yield the highest P/depth estimates beneath most of the arc, followed by IPB types, then calcalkalic basalts (CA), basaltic andesites (BA), and shoshonites (SHO) at progressively shallower depths. Elevated isotherms in the upper mantle wedge are consistent with long-term infiltration by hot basaltic magmas (cf. Rees Jones et al., 2018). Locus of the subducting slab surface (thick blue curve) at 46°N is approximate owing to poor seismic resolution at depths greater than ca. 40-60 km (cf. McCrory et al., 2012). Reconciliation of inferred magma segregation depths and subduction zone geometry is discussed by Leeman et al. (2005), but remains unresolved. Right panel shows inferred depth relations for MSH lavas as described here (Supplement Table A5) and incorporating other petrologic (Pallister et al., 2008; Wanke et al., 2016; Zellmer et al., 2016; Blatter et al., 2017) and geophysical (Miller et al., 1997; Kiser et al., 2016) constraints. The presence of mantle-derived basalts (LKT, hy- and ne-IPB) below 30 km is speculative, but consistent with depths calculated (with no olivine addition) for primitive CCT basalts and high-Vp seismic zones interpreted as cumulates (Kiser et al., 2016). These basalts presumably provided heat for melting crustal source rocks, generating dacitic liquids (Blatter et al., 2017). Derivatives of these basaltic magmas, slightly modified, were stored in slightly shallower reservoirs (A and B1) from which the most primitive MSH lavas erupted. These basalts in turn interacted to varying degree with crustal wall rocks, other more evolved magmas, and/or crystal mush zones to generate the erupted spectrum of basalts and basaltic andesites. Schematic storage zones and vertical conduits for these magmas (e.g., B2-S, B2-N, etc.) are depicted based on inferred pressures from our work. Although these magma reservoirs appear to be separated by depth, it is also possible that distinct storage zones and conduits were horizontally separated beneath MSH. The figure also illustrates the location of the 1980 shallow dacitic magma reservoir based on petrologic and seismic studies (Pallister et al., 1992 and references therein). During Castle Creek time, dacitic "traps" were apparently inefficient in preventing eruption of mafic magmas, perhaps because they were relatively small in volume and/or spatial extent.

23

Although primitive regional LKT and IPB magmas are inferred to have low water contents, estimated water contents in more evolved MSH mafic lavas generally exceed levels predicted by fractional crystallization models (cf. Figure 14 and Supplement Table A5) and cannot be explained by formation of crystals alone. However, water contents are rather well correlated with independently estimated weight fractions of 'andesitic component' inferred from our mixing models; this implies that water contents were in some manner embellished by external inputs during magma ascent and/or storage. The least evolved samples of Groups A and B1 produce remarkably consistent estimates for temperature and depth, and we consider these to correspond to different domains of magma injection in the deep crust. Based on our mixing calculations and the apparent 'excess water' in many samples, we infer that the magmas must have interacted with preexisting water-rich wall rocks or more water-rich melts. Possible sources of 'external water' are amphibolitic crustal rocks and/or melts produced by dehydration melting of such rocks (cf. Ankney et al., 2013, and references therein). The more evolved lavas of Groups A and B2 seem to have resided for part of their history in shallower and cooler zones where interaction with 'andesitic components' was more extensive. This interaction obviously modified magmatic compositions (cf. Hildreth and Moorbath, 1988; Solano et al, 2014; Zellmer et al., 2016). An important consequence is that magmatic densities were correspondingly reduced, and this could have affected the buoyancy of a given magma parcel, hence its depth of neutral buoyancy in a density stratified magmatic conduit system.

The importance of magmatic density

Densities of MSH magmas (calculated on both hydrous and anhydrous bases; Supplement Note 5 and Table A5; cf. Bottinga and Weill, 1970) correlate strongly with SiO_2 content, reservoir depth, and estimated weight fraction of an 'andesitic' component (Fig. 14). Thus, we envisage that as parental basaltic magmas progressively mingle with and/or assimilate preexisting magmatic components in the deep crust, resulting hybridized magmas will ascend and concentrate toward shallower depths. The magnitude of their ascent may be dictated by their density and the density contrast with pre-existing crust/wall rocks. As successive magma batches solidify, they will increase the local

density of the crust such that later intrusive batches can achieve neutral buoyancy at progressively shallower depths over time (cf. Leeman et al., 2008). In this manner, the magma plexus could develop a gradational structure with least evolved (i.e., denser) mafic magmas concentrated toward deeper levels and more evolved magmas distributed at shallower depths.

The most primitive LKT and IPB magmas have densities near 2.85 kg/m^3, and would have difficulty rising far into the crust unless its density was increased (e.g., due to solidification of prior intrusions). This view is consistent with our estimated depths (31-34 km for primitive LKT and ne-IPB of the CCT; 28 km for Group B1, and 23 km for Group A). Moreover, density-controlled stratification could explain how the different magma types remained isolated while they resided in their respective crustal 'reservoirs' (Fig. 15). The shallower Group A 'reservoir' might be more likely to interact with the overlying magmatic plexus, which could help explain elevated water contents in these lavas. The top of the magmatic plexus could be controlled by the shallowest depth for neutral buoyancy, which will depend on the density of magmas stored at those levels. Because the most evolved mafic magmas of Groups A and B have estimated densities of ~2.6 kg/m^3 (as do two low silica andesites), it is unlikely that they could ascend solely by buoyancy to depths shallower than about 15 km (above which lies the inferred lower-density dacitic reservoir). We expect that more silicic andesitic and dacitic magmas would have substantially lower densities (~2.5-2.4 kg/m^3, depending on water content), and would collect at depths shallower than the mafic-dominated parts of the magma system. This is in accord with seismologic and petrologic interpretations that the historically erupted MSH dacites are extracted from a conduit system at depths between 5-15 km (Pallister et al., 2008; Rutherford and Devine, 2008; Blundy et al., 2008; Blatter et al., 2017, and references therein). Magma mixing could transpire in the intervening region (i.e., 23-15 km depths) between basalt accumulation zones deep in the crust and dacite accumulation zones in the shallow crust, where intermediate composition magma, crystal mushes, thawed earlier intrusions, and/or dacitic crustal melts could contribute to the 'andesitic' component. Collectively, the entire MSH magmatic plumbing system is visualized as being of crustal scale (cf. Cashman et al., 2017), with periodic inputs of basaltic magmas from the upper mantle.

Some loose ends

Lingering questions concern what actually triggers eruptions, and how geochemical identities of LKT and IPB magma lineages remain distinct. In the above scenario, we stress the hydrostatic factors that influence magma migration. In isolation, the denser mafic lavas would have insufficient buoyancy to ascend through less dense crust and reach the surface. This impediment could be overcome in two ways. First, an eruptible magma column can be sustained if it is deeply rooted in the upper mantle. This presumably is a requirement for eruption of dense, primitive basalt types. However, if magma supply from depth is interrupted, isolated magma batches will tend to accumulate at depths where they become neutrally buoyant (as discussed above). In this case, a secondary trigger is required to initiate eruptions. This could be due to expansion of volatile components released by either decompression of magma or heating in response to new inputs of ascending hot magma (cf. Sparks et al., 1977; Eichelberger and Izbekov, 2000; Annen et al., 2006; Solano et al., 2012; Parmigiani et al., 2014; Girona et al., 2015). We envisage that both processes are plausible at MSH. The accumulation of 'excess' water content in the evolved mafic lavas during crustal storage would enhance their eruptability, especially if suitable dike-like conduits can form. Tectonic pressurization is another potential trigger for basaltic eruption (cf. Manga and Brodsky, 2006; Nishimuri, 2017), but difficult to assess for MSH.

That distinct magma types appear to be localized at specific vent areas suggests that conduit formation must initiate proximal to a given deep crustal reservoir, then propagate to the surface without significantly interacting with other distinctive reservoirs (cf. Spiegelman et al., 2001). Preservation of textural features such as the 'rhyolitic' melt bleb in DS-4 implies rapid ascent of this batch of basalt following a magma mingling event. Also, upward increasing MgO content in the North flank basalt sequences, as well as the observed mixing arrays, could represent a sequential purging of the respective feeder conduits in which the earliest erupted material had been modified to greater extent by interactions during ascent. Such conduit geometry seems to be required during Castle Creek time, but this may not have always been the case. For example, the prevalence of

andesitic and more silicic magmas during other eruptive periods at MSH, or at other arc volcanoes, may be a consequence of more efficient mixing.

Comparisons with other volcanic systems

Fifty years ago, McBirney (1968) highlighted a dichotomy in Cascades stratovolcanoes in that some (e.g., Hood, Rainier) erupt relatively monotonous andesitic to dacitic magmas, whereas others (Adams, Mazama) are characterized by a broad spectrum of magmas ranging from basalt to rhyolite. Mount St. Helens is somewhat exceptional in that its predominantly andesite-dacite eruptions were augmented by basaltic activity only during the Castle Creek period. This latter excursion presumably was a response to a transient change in the underlying magmatic conduit system. Examples from other volcanoes help put this into perspective.

In a study of nearby Mount Hood, Kent (2014) concludes that andesites and other intermediate magmas are plausibly produced by a number of mechanisms. However, a lack of evidence for actual andesitic liquids viz. a viz. the abundance of andesitic volcanic rocks at Mt. Hood (also worldwide; Naumov et al., 1997; Reubi and Blundy, 2009), together with widespread evidence for hybridization and recharge, suggests that many (most?) erupted andesites form by mixing between relatively mafic magmas of ultimate mantle derivation and more felsic magmas or mush zones derived from differentiation and crustal melting. A model of recharge filtering can account for the high abundance of andesitic volcanic rocks and is based on the simple notion that the processes that create hybridized andesitic magmas in the shallow crust can also initiate volcanic activity, resulting in preferential eruption of andesitic magmas relative to the parental magmas that mix to produce them. This plausibly occurs via mafic recharge – i.e., intrusion of a mafic magma into a silicic magma or mush within the shallow crust. This idea is supported at MSH by observations of complex mingling of distinctive intermediate and high-SiO_2 glasses preserved in Kalama age scoria samples from the north flank of MSH (Pallister et al., 2008; Wackett and Smith, 2013), by the silicic melt 'bleb' preserved in our DS-4 basaltic lava, and by the complexity of olivine core populations documented in this study. There are numerous other examples where this phenomenon seems to prevail (e.g., Borg and Clynne, 1998; Eichelberger and Izbekov,

2000; Kent et al., 2010; Baggerman and DeBari, 2011; Price et al., 2012; Humphreys et al., 2013; Sisson et al., 2014).

The presence of shallow silicic magma bodies is likely to play a significant role in the behavior of many volcanoes (cf. Eichelberger et al., 2006). For example, Karlstrom et al. (2015) argue that the spatial and temporal distribution of geographically clustered volcanic vents near Mt. Mazama reflects the development of a centralized magma chamber that fed the climactic eruption. Time-averaged eruption rates there imply an order of magnitude increase in deep magma influx prior to the caldera-forming event, suggesting that an increase in melt productivity could have triggered a chamber growth episode. They modeled magma chamber-dike interactions preceding the climactic eruption and predicted that expansion of the shallow magma chamber effectively forced proximal mafic vent locations to migrate away from the climactic eruptive center, only to return to the original areas after the shallow silicic magma chamber was evacuated by the caldera-forming eruption. Albeit smaller in scale than Mazama, the persistent effusion of dacitic magmas at MSH over 300 ka is consistent with a long-lived shallow magma system, and periodic andesite eruptions can be explained by efficient interception of basaltic magmas by this system (Pallister et al., 2008). The appearance of significant basaltic magmatism only at Castle Creek time likely signifies that the shallow silicic part of the system had waned (solidified) to the point that it was no longer an efficient magma trap, allowing brittle deformation and development of through-going conduits for deep-seated (mantle or deep-crust derived) magmas to reach the surface during this time interval.

Comparative plots of MgO vs. K_2O for selected Cascades stratovolcanoes (Fig. 16) provide hints that, as at MSH, inputs of diverse basaltic magmas occurred sporadically and mixed with more evolved magmas stored in the local feeder systems. At Mt. Adams, at least three potential mixing arrays can be discerned with probable inputs of LKT, IPB, and a potassic IPB similar to lavas from the nearby Simcoe volcanic field to the east (cf. Leeman et al., 1990). Without detailed chronologic information, it is difficult to discern whether these individual trends represent single mixing episodes, or whether similar mixing end members are involved in some recurring fashion. Even for Mt. Hood, originally considered to be a 'coherent volcano' by McBirney (1968), the currently

28

available data show vestiges of a mixing array - in this case with input of IPB-type magma. These observations imply that, at least intermittently, there are widespread inputs of primitive basaltic magmas of several distinctive varieties that have ascended beneath the CCT – in essence, a 'mantle wind' that ultimately drives shallower volcanic processes. The full magnitude and nature of these deep magmatic components commonly are obscured and underestimated due to interactions within the crust beneath the stratovolcanoes. Recognition of this problem has stimulated the investigation of small eruptive centers peripheral to large stratovolcanoes (e.g., Leeman et al, 2005; Rowe et al., 2009; McGee et al., 2017).

Relevance to distribution and mechanisms of melt production

There has been reinvigorated interest in the distribution of melt production beneath the Cascades arc, and the region around MSH in particular. Monitoring of seismic activity prior to and following the eruptions of MSH since 1980 provides clear evidence that dacitic eruptions were sourced from magma reservoirs at depths between ~7-15 km beneath the volcano (Lees, 1992; Musumeci et al., 2002**).** These depths are consistent with petrologic and other constraints (cf. Pallister et al., 2008; Blatter et al., 2017) and our observations. The widespread distribution of small monogenetic vents and lava fields across the CCT implies that melting has occurred at least sporadically across the entire region, extending well into the frontal arc region (Leeman et al., 2005; Evarts et al., 2017). Magnetotelluric sounding studies demonstrate that much of the region is characterized by high electrical conductivity with highest values imaged beneath the most recently active volcanic features (Hill et al., 2009; Meqbel et al., 2014). Active seismic studies (Hansen et al. 2016; Kiser et al., 2016) have identified relatively low velocity regions that broadly coincide with the high conductivity domains, as well as higher velocity domains in the lower crust that are attributed to mafic intrusions at depths near the base of our inferred deepest basaltic reservoir. In general, all of these approaches emphasize crustal features and, so far, lack sufficient resolution to provide detailed information about sub-Moho processes or mantle thermal structure. Authors of the latter studies have suggested that mafic magmas feeding the MSH conduit system have migrated laterally from easterly locales (e.g., Indian Heaven volcanic field). In contrast,

29

our work suggests that basaltic magmas ascend more or less directly from upper mantle depths below the volcano. Otherwise, it is difficult to explain how magmas from closely proximal vents could preserve the observed diversity if their transport involved significant lateral migration in a long horizontal flow regime.

IMPLICATIONS

This paper addresses the contributions of mantle-derived basaltic magmas to the long-lived MSH volcano, including where they originate, how they ascend, and why they rarely erupt. Basaltic eruptions occurred only during a short ~200 year period within the Castle Creek eruptive stage (~2100-1800 yrs. B.P.), and thus provide a brief snapshot of the overall evolution of its magmatic system. Key findings include the following: [1] there are two distinct basaltic lineages, both of 'intraplate' magmatic affinity – one of low-K tholeiite, the other similar to ocean island basalts, [2] compositional variations in both suites of mafic lavas are strongly influenced by mixing with material akin to average MSH andesite, and [3] primitive and derivative lavas from each suite seem to have distinct storage reservoirs and conduit systems that are distributed throughout the deep and middle crust. Our estimates of physical conditions and compositional evolution provide exciting new insights into the structure of the underlying crustal-scale magmatic complex. We propose that depths of magma emplacement are controlled primarily by magma density that, in turn, is determined by the extent of interaction between the basaltic magmas and more evolved magmas and other crustal components during ascent and storage. This concept is applicable to varying degree to virtually all types of volcanoes. An important implication is that processes beneath large stratovolcanoes can strongly modify mantle-derived magmas, obscure aspects of their primary characteristics, and bias perceptions of their petrogenesis.

ACKNOWLEDGEMENTS

analyses), and Donggao Zhao (EMP analyses).   We thank Keith Putirka, David Neave, Dan Kelley, Laura Waters, and Andrew Berry for information and advice.   We also thank Frank Tepley, Lucy McGee, and editor Susanne Straub for their positive reviews and suggestions that greatly improved the presentation of this work.   Finally, we thank the University of Texas for access to their EMP, and the W.M. Keck Foundation for funding for acquisition of the Trinity University SEM.   This work was partly funded by research grants to WPL from the National Science Foundation.   DRS thanks Trinity University for support from faculty development funds.

REFERENCES CITED

Anderson, A.T. (1976) Magma mixing: Petrological process and volcanological tool. Journal of Volcanology and Geothermal Research, 1, 3-33.

Ankney, M.E., Johnson, C.M., Bacon, C.R., Beard, B.L., and Jicha, B.T. (2013) Distinguishing lower and upper crustal processes in magmas erupted during the buildup to the 7.7 ka climactic eruption of Mount Mazama, Crater Lake, Oregon, using ^{238}U-^{230}Th disequilibria. Contributions to Mineralogy and Petrology, 166:563-585, doi:10.1007/s00410-013-0891-4.

Annen, C., Blundy, J.D., and Sparks, R.S.J. (2006) The genesis of intermediate and silicic magmas in deep crustal hot zones. Journal of Petrology, 47, 505–539, doi:10.1093/petrology/egi084.

Bacon, C.R. (1990) Calc-alkaline, shoshonitic, and primitive tholeiitic lavas from monogenetic volcanoes near Crater Lake, Oregon. Journal of Petrology, 31, 135-166.

Bacon, C.R., Bruggman, P.E., Christiansen, R.L., Clynne, M.A., Donnelly-Nolan, J.M., and Hildreth, W. (1997) Primitive magmas at five Cascade volcanic fields: Melts from hot, heterogeneous sub-arc mantle. Canadian Mineralogist, 35, 397-423.

Baggerman, T.D., and DeBari, S.M. (2011) The generation of a diverse suite of Late Pleistocene and Holocene basalt through dacite lavas from the northern Cascade arc at Mount Baker, Washington. Contributions to Mineralogy and Petrology, 161, 75-99.

Beier, C., Haase, K.M., Brandl, P.A., and Krumm, S.H. (2017) Primitive andesites from the Taupo Volcanic Zone formed by magma mixing. Contributions to Mineralogy and Petrology, 172:33, doi: 10.1007/s00410-017-1354-0.

Blatter, D.L., Sisson, T.W., and Hankins, W.B. (2017) Voluminous arc dacites as amphibole reaction-boundary liquids. Contributions to Mineralogy and Petrology, 172:27, doi:10.1007/s00410-017-1340-6.

Blundy, J., Cashman, K.V., and Berlo, K. (2008) Evolving magma storage conditions beneath Mount St. Helens inferred from chemical variations in melt inclusions from the 1980–1986 and current (2004–2006) eruptions. In D.R. Sherrod, W.E. Scott, W.E., and P.H. Stauffer, Eds., A volcano rekindled: The renewed eruption of Mount St. Helens, 2004–2006. U.S. Geological Survey Professional Paper 1750, p. 755-790.

Borg, L.E. and Clynne, M.A. (1998) The petrogenesis of felsic calc-alkaline magmas from the southernmost Cascades, California – Origin by partial melting of basaltic lower crust. Journal of Petrology, 39, 1197-1222.

Borg, L.E., Clynne, M.A., and Bullen, T.D. (1997) The variable role of slab-derived fluids in the generation of a suite of primitive calc-alkaline lavas from the southernmost Cascades, California. Canadian Mineralogist, 35, 425-452.

Bostock, M., Hyndman, R.D., Rondenay, S., and Peacock, S.M. (2002) An inverted continental Moho and serpentinization of the forearc mantle. Nature, 417, 536-538, doi:10.1038/417536a.

Bottinga, Y., and Weill, D.F. (1970) Densities of liquid silicate systems calculated from partial molar volumes of oxide components. American Journal of Science, 269, 169-182.

Brocher, T.M., Parsons, T., Tréhu, A.M., Snelson, C.M., and Fisher, M.A. (2003) Seismic evidence for widespread serpentinized forearc upper mantle along the Cascadia margin. Geology, 31, 267-270.

Carroll, K.R. (2009) Mixing components and dynamics of Kalama Period intermediate magmas at Mount St. Helens: Evidence from mafic phenocrysts. M.S. thesis, Portland State University, Oregon, 305 p.

Carroll, K.R., Streck, M.J., Pallister, J.S., and Leeman, W.P. (2008) Interaction of dacitic and basaltic magmas deduced from evolution of phenocrysts and mixing of crystal populations during the Kalama eruptive period, Mount St. Helens. EOS, American Geophysical Union, Fall Meeting, Abstract V23E-2175.

Carroll, K.R., Streck, M.J., Pallister, J.S., and Leeman, W.P. (2009) Mixing components and hybridization processes of Kalama period intermediate magmas from Mount St. Helens: Evidence from mafic phenocrysts. Geological Society of America Abstracts with Programs, 41, no. 7, 190.

Cashman K.V., Sparks R.S.J., and Blundy J.D. (2017) Vertically extensive and unstable magmatic systems: A unified view of igneous processes. Science, 355, eaag3055, doi:10.1126/science.aag3055.

Clynne, M., Champion, D., and Wanke, M. (2017) Stratigraphy and age of the Castle Creek eruptive period, Mount St. Helens, Washington. International Association for Volcanology and Chemistry of the Earth's Interior General Session, Portland, OR, Abstract 506.

Clynne, M.A., Champion, D.E., Wolfe, E.W., Gardner, C.A., and Pallister, J.S. (2004) Stratigraphy and paleomagnetism of the Pine Creek and Castle Creek eruptive episodes, Mount St. Helens, Washington. EOS, American Geophysical Union, Fall Meeting 2004, Abstract V43E-1453.

Clynne, M.A., Calvert, A.T., Wolfe, E.W., Evarts, R.C., Fleck, R.J., and Lanphere, M.A. (2008) The Pleistocene eruptive history of Mount St. Helens, Washington, from 300,000 to 12,800 years before present. In D.R. Sherrod, W.E. Scott, W.E., and P.H. Stauffer, Eds., A volcano rekindled: The renewed eruption of Mount St. Helens, 2004–2006. U.S. Geological Survey Professional Paper 1750, p. 593-627.

Conrey, R.M., Sherrod, D.R., Hooper, P.R., and Swanson, D.A. (1997) Diverse primitive magmas in the Cascade arc, northern Oregon and southern Washington. Canadian Mineralogist, 35, 367-396.

Conrey, R.M., Evarts, R.C., Leeman, W.P., Streck, M.J., and Fleck, R.J. (2009) A petrologic overview of the Boring Volcanic Field, Cascade Range, USA. Geological Society of America Abstracts with Programs, 41, no. 7, 190.

Costa, F., Andreastuti, S., Vouvet de Maisonneuve, C., and Pallister, J.S. (2013) Petrological insights into the storage conditions, and magmatic processes that yielded the centennial 2010 Merapi explosive eruption. Journal of Volcanology and Geothermal Research, 261, 209-235, doi: 10.1016/jvolgeores.2012.12.025.

Donnelly-Nolan, J.M., Champion, D.E., Grove, T.L., Baker, M.B., Taggert, J.E., and Bruggman, P.E. (1991) The Giant Crater lava field: Geology and geochemistry of a compositionally zoned, high-alumina basalt to basaltic andesite eruption at Medicine Lake volcano, California. Journal of Geophysical Research, 96(B15), 21843-21863, doi:1029/91JB01901.

Eichelberger, J.C., and Izbekov, P.E. (2000) Eruption of andesite triggered by dyke injection: Contrasting cases at Karymsky volcano, Kamchatka and Mt Katmai, Alaska. Philosophical Transactions of the Royal Society of London, 358, 1465-1485.

Eichelberger, J.C., Izbekov, P.E. and Browne, B.L. (2006) Bulk chemical trends at arc volcanoes are not liquid lines of descent. Lithos 87, 135-154.

Eiler, J.M. (2001) Oxygen isotope variations of basaltic lavas and upper mantle rocks. Reviews in Mineralogy and Geochemistry, 43, 319-364, doi:10.2138/gsrmg.43.1.319.

Evarts, R.C., Conrey, R.M., Leeman, W.P., and Streck, M.J. (2017) Insights into magmatic diversity in the Columbia Cascades Transect (CCT). International Association of Volcanology and Chemistry of the Earth's Interior General Session, Portland, OR, Abstract 1232.

Garcia, M.O. (1996) Petrography and olivine and glass chemistry of lavas from the Hawaii Scientific Drilling Project. Journal of Geophysical Research, 101, 11701-11713.

Gardner, J.E., Carey, S., Rutherford, M.J., and Sigurdsson, H. (1995) Petrologic diversity in Mount St. Helens dacites during the last 4,000 years; implications for magma mixing. Contributions to Mineralogy and Petrology, 119, 224-238.

Girona, T., Costa, F., and Schubert, G. (2015) Degassing during quiescence as a trigger of magma ascent and volcanic eruptions. Scientific Reports, 5, 18212, doi:10.1038/srep18212.

Greeley, R., and Hyde, J.H. (1972) Lava tubes of the Cave Basalt, Mount St. Helens, Washington. Geological Society of America Bulletin, 83, 2397-2418.

Green, N.L. (1988) Basalt-basaltic andesite mixing at Mount Baker Volcano, Washington: 1. Estimation of mixing conditions. Journal of Volcanology and Geothermal Research, 34, 251-265.

Green, N.L. (2006) Influence of slab thermal structure on basalt source regions and melting conditions: REE and HFSE constraints from the Garibaldi volcanic belt, northern Cascadia subduction system. Lithos, 87, 23-49.

Grove, T.L., Parman, S.W., Bowring, S.A., Price, R.C., and Baker, M.B. (2002) The role of an H_2O-rich fluid component in the generation of primitive basaltic andesites and andesites from the Mt. Shasta region, N California. Contributions to Mineralogy and Petrology, 142, 375-396, doi:10.1007/s004100100299.

Hagstrum, J.T., Hoblitt, R.P., Gardner, C.A., and Gray, T.E. (2002) Holocene geomagnetic secular variation recorded by volcanic deposits at Mount St. Helens, Washington. Bulletin of Volcanology, 63, 545-556.

Halliday, A.N., Fallick, A.E., Dickin, A.P., Mackenzie, A.B., Stephens, W.E., and Hildreth, W. (1983) The isotopic and chemical evolution of Mount St. Helens. Earth and Planetary Science Letters, 63, 241-256.

Hansen, S.M., Schmandt, B., Levander, A., Kiser, E., Vidale, J.E., Abers, G.A., and Creager, K.C. (2016) Seismic evidence for a cold serpentinized mantle wedge beneath Mount St Helens. Nature Communications, 7, doi:10.1038/ncomms13242.

Harry, D.L., and Green, N.L. (1999) Slab dehydration and basalt petrogenesis in subduction systems involving very young oceanic lithosphere. Chemical Geology, 160, 309-333.

Heliker, C.C. (1995) Inclusions in Mount St. Helens dacite erupted from 1980 to 1983. Journal of Volcanology and Geothermal Research, 66, 115-135.

Hildreth, W. (2007) Quaternary magmatism in the Cascades – geologic perspectives. U.S. Geological Survey Professional Paper, 1744, 125 p.

Hildreth, W., and Moorbath, S. (1988) Crustal contributions to arc magmatism in the Andes of Central Chile. Contributions to Mineralogy and Petrology, 98, 455-489, http://dx.doi.org/10.1007/BF00372365

Hildreth, W., and Fierstein, J. (1997) Recent eruptions of Mount Adams, Washington Cascades, USA. Bulletin of Volcanology, 58, 472-490.

Hill, G.J., Caldwell, T.G., Heise, W., Chertkoff, D.G., Bibby, H.M., Burgess, M.K., Cull, J.P., and Cas, R.A.F. (2009) Distribution of melt beneath Mount St. Helens and Mount

35

Adams inferred from magnetotelluric data. Nature Geoscience, 2, 785-789, doi:10.1038/NGEO661.

Hirschmann, M.M. (2000) Mantle solidus: Experimental constraints and the effects of peridotite composition. Geochemistry, Geophysics, Geosystems, 1, 1042, doi:10.1029/2000GC000070.

Hopson, C.A. (2008) Geologic map of Mount St. Helens, Washington prior to the 1980 eruption. U.S. Geological Survey Open-File Report 02-468, version 1.

Horodyskyj, U., Lee, C.-T.A., and Luffi, P. (2009) Geochemical evidence for exhumation of eclogite via serpentinite channels in ocean-continent subduction zones. Geosphere, 5, 426-438, doi: 10.1130/GES00502.1.

Humphreys, M.C.S., Edmonds, M., Plail, M., Barclay, J., Parkes, D., and Christopher, T. (2013) A new method to quantify the real supply of mafic components to a hybrid andesite. Contributions to Mineralogy and Petrology, 165, 191-215.

Jicha, B.R., Hart, G.L., Johnson, C.M., Hildreth, W., Beard, B.L., Shirey, S.B., and Valley, J.W. (2009) Isotopic and trace element constraints on the petrogenesis of lavas from the Mount Adams volcanic field, Washington. Contributions to Mineralogy and Petrology, 157, 189-207.

Johnson, D.M., Hooper, P.R., and Conrey, R.M. (1999) XRF analysis of rocks and minerals for major and trace elements on a single low dilution Li-tetraborate fused bead. Advances in X-ray Analysis 41, 843-867.

Karlstrom, L., Wright, H.M., and Bacon, C.R. (2015) The effect of pressurized magma chamber growth on melt migration and pre-caldera vent locations through time at Mount Mazama, Crater Lake, Oregon. Earth and Planetary Science Letters, 412, 209-219, doi:10.1016/j.epsl.2014.12.001.

Kent, A.J.R. (2014) Preferential eruption of andesitic magmas: Implications for volcanic magma fluxes at convergent margins. In A. Gómez-Tuena, S,M. Straub, and G.F. Zellmer, Eds., Orogenic andesites and crustal growth. Geological Society of London Special Publications, 385, 257-289, doi.org/10.1144/SP385.10.

Kent, A.J.R., Darr, C., Koleszar, A.M., Salisbury, M., and Cooper, K.M. (2010) Preferential eruption of andesitic magmas through recharge filtering. Nature Geoscience, 3, 631-636, doi:10.1038/ngeo924.

Kiser, E., Palomeras, I., Levander, A., Zelt, C., Harder, S., Schmandt, B., Hansen, S., Creager, K., and, Ulberg, C. (2016) Magma reservoirs from the upper crust to the Moho inferred from high-resolution Vp and Vs models beneath Mount St. Helens, Washington State, USA. Geology 44, 411-414, doi:10.1130/G37591.1.

Knaack, C., Cornelius, S.B., and Hooper, P.R. (1994) Trace element analyses of rocks and minerals by ICP-MS. Technical Notes, GeoAnalytical Lab, Washington State University, https://environment.wsu.edu/facilities/geoanalytical-lab/technical-notes/icp-ms-method/.

Le Voyer, M., Rose-Koga, E.F., Shimizu, N., Grove, T.L., and Schiano, P. (2010) Two contrasting H_2O-rich components in primary melt inclusions from Mount Shasta. Journal of Petrology, 51, 1571-1595.

Lee, C.-T.A., Luffi, P., Plank, T., Dalton, H., and Leeman, W. (2009) Constraints on the depths and temperatures of basaltic magma generation on Earth and other terrestrial planets using new thermobarometers for mafic magmas. Earth and Planetary Science Letters, 279, 20-33, doi:10.1016/j.epsl.2008.12.020.

Lee, C.-T.A., Luffi, P., Le Roux, V., Dasgupta, R., Albaréde, F., and Leeman, W.P. (2010) The redox state of arc mantle using Zn/Fe systematics. Nature, 468, 681-685, doi:10.1038/nature09617.

Leeman, W.P., Annen, C., and Dufek, J. (2008) Snake River Plain – Yellowstone silicic magmatism: Implications for magma genesis and magma fluxes. In C. Annen, and G.F. Zellmer, Eds., Dynamics of crustal magma transfer, storage, and differentiation. Geological Society of London Special Publications, 304, 235-259.

Leeman, W.P., Tonarini, S., Chan, L.H., and Borg, L.E. (2004) Boron and lithium isotopic variations in a hot subduction zone – the southern Washington Cascades. Chemical Geology, 212, 101-124.

Leeman, W.P., Smith, D.R., Hildreth, W., Palacz, Z., and Rogers, N. (1990) Compositional diversity of Late Cenozoic basalts in a transect across the southern Washington Cascades: Implications for subduction zone magmatism. Journal of Geophysical Research, 95, 19561-19582.

Leeman, W.P., Lewis, J.F., Evarts, R.C., Conrey, R.M., and Streck, M.J., (2005) Petrologic constraints on the thermal structure of the Cascades arc. Journal of Volcanology and Geothermal Research, 140, 67-105.

Lees, J.M. (1992) The magma system of Mount St. Helens: Non-linear high resolution P-wave tomography. Journal of Volcanology and Geothermal Research, 53, 103–116.

Lewis, J.F. (2004) Investigation on the generation of primitive basalts in the southern Washington Cascades. M.A. thesis, Rice University, 127 p.

Lieuallen, A.E., Tepley, F.J., and Clynne, M.A. (2009) Magmatic interactions on short time scales: magma mixing during the Kalama eruptive period at Mount St. Helens, Washington. EOS, American Geophysical Union, Fall Meeting 2009, Abstract V43B-2239.

Lopez-Escobar, L., Frey, F.A., and Vergera, M. (1977) Andesites and high-alumina basalts from the central-south Chile High Andes: Geochemical evidence bearing on their petrogenesis. Contributions to Mineralogy and Petrology, 63, 199-228.

Maclennan, J., McKenzie, D., Grönvold, K., Shimizu, N., Eiler, J.M., and Kitchen, N. (2003) Melt mixing and crystallization under Theistareykir, northeast Iceland. Geochemistry Geophysics Geosystems, 4, 8624, doi:10.1029/2003GC000558.

Manea, V.C., Leeman, W.P., Gerya, T., Manea, M., and Zhu, G. (2014) Subduction of fracture zones controls mantle melting and geochemical signature above slabs. Nature Communications, 5, 5095, doi:10.1038/ncomms6095.

Manga, M., and Brodsky, E. (2006) Seismic triggering of eruptions in the far field: Volcanoes and geysers. Annual Review of Earth and Planetary Sciences, 34, 263-291, doi:10.1146/annurev.earth.34.031405.125125..

Mattos, S.T. (2006) Deciphering the signature of magma mixing: Examples from the Castle Creek eruptive period, Mount St. Helens, Washington. M.S. thesis, Central Washington University, 132 p.

McBirney, A.R. (1968) Petrochemistry of the Cascade andesite volcanoes. Oregon Department of Geology and Mineralogy Industry Bulletin, 62, 101-107.

McCrory, P.A., Blair, J.L., Waldhauser, F., and Oppenheimer, D.H. (2012) Juan de Fuca slab geometry and its relation to Wadati-Benioff zone seismicity. Journal of Geophysical Research, 117, B09306, doi:10.1029/2012JB009407.

McGee, L.E., Braham, R., Rowe, M.C., Handley, H.K., Morgado, E., Lara, L.E., Turner, M.B., Vinet, N., Parada, M.-A., and Valdivia, P. (2017) A geochemical approach to distinguishing competing tectono-magmatic processes preserved in small eruptive centers. Contributions to Mineralogy and Petrology, 172:44, doi:10.1007/s00410-017-1360-2.

Médard, E., and Grove., T.L. (2008) The effect of H_2O on the olivine liquidus of basaltic melts: experiments and thermodynamic models. Contributions to Mineralogy and Petrology 155, 417-432, doi:10.1007/s00410-007-0250-4.

Meqbel, N.M., Egbert, G.D., Wannamaker, P.E., Kelbert, A., and Schultz, A. (2014) Deep electrical resistivity structure of the northwestern U.S. derived from 3-D inversion of USArray magnetotelluric data. Earth and Planetary Science Letters, 402, 290-304, doi:10.1016/j.epsl.2013.12.026.

Miller, K.C., Keller, G.R., Gridley, J.M., Luetgert, J.H., Mooney, W.D., and Thybo, H. (1997) Crustal structure along the west flank of the Cascades, western Washington. Journal of Geophysical Research, 102, 17857-17873.

Miyashiro, A. (1974) Volcanic rock series in island arcs and active continental margins. American Journal of Science, 274, 321-355.

Mullineaux, D.R., and Crandell, D.R. (1981) The eruptive history of Mount St. Helens. In: P.W. Lipman, and D.R. Mullineaux, Eds., The 1980 eruptions of Mount St. Helens, Washington. U.S. Geological Survey Professional Paper 1250, 3-15.

Musumeci, C., Gresta, S., and Malone, S.D. (2002) Magma system recharge of Mount St. Helens from precise relative hypocenter location of microearthquakes. Journal of Geophysical Research, 107(B10), 2264, doi:10.1029/2001JB000629.

Naumov, B.V., Kovalenko, V.I., Babansky, A.D., and Tolstykh, M.L. (1997) Genesis of andesites: Evidence from studies of melt inclusions from minerals. Petrology, 5, 586-596.

Newman, S., and Lowenstern, J.B. (2002) VOLATILECALC: A silicate melt-H_2O-CO_2 solution model written in Visual Basic for excel. Computers & Geosciences, 28, 597-604.

Nishimuri, T. (2017) Triggering of volcanic eruptions by large earthquakes. Geophysical Research Letters, 44, 7750-7756, doi:10.1002/2017GL074579.

39

Norman, M.D., Leeman, W.P., Blanchard, D.P., and Fitton, J.G. (1989) Comparison of major and trace element analyses by ICP, XRF, INAA, and ID methods. Geostandards Newsletter, 13, 283-290.

Oeser, M., Ruprecht, P., and Weyer, S. (2018) Combined Fe-Mg chemical and isotopic zoning in olivine constraining magma mixing-to-eruption timescales for the continental arc volcano Irazu (Costa Rica) and Cr diffusion in olivine. American Mineralogist, 103, 582-599, doi:10.2138/am-2018-6258.

Pallister, J.S., Hoblitt, R.P., Crandell, D.R., and Mullineaux, D.R. (1992) Mount St. Helens a decade after the 1980 eruptions: Magmatic models, chemical cycles, and a revised hazards assessment. Bulletin of Volcanology, 54, 126-146.

Pallister, J.S., Thornber, C.R., Cashman, K.V., Clynne, M.A., Lowers, H.A., Mandeville, C.W., Brownfield, I.K., and Meeker, G. (2008) Petrology of the 2004-2006 Mount St. Helens lava dome: Implications for magmatic plumbing and eruption triggering. In D.R. Sherrod, W.E. Scott, W.E., and P.H. Stauffer, Eds., A volcano rekindled: The renewed eruption of Mount St. Helens, 2004–2006. U.S. Geological Survey Professional Paper 1750, p. 647-702.

Pallister, J.S., Clynne, M.A., Wright, H.M., van Eaton, A.R., Vallance, J.W., Sherrod, D.R., and Kokelaar, B.P. (2017) Field trip guide to Mount St. Helens, Washington – An overview of the eruptive history and petrology, tephra deposits, 1980 pyroclastic density current deposits, and the crater. U.S. Geological Survey Scientific Investigations Report 2017–5022–D, 65 p., https://doi.org/10.3133/sir20175022D.

Parmigiani, A., Huber, C., and Bachmann, O. (2014) Mush microphysics and the reactivation of crystal-rich magma reservoirs. Journal of Geophysical Research, 119, 6308–6322, doi:10.1002/2014JB011124.

Plank, T., and Forsyth, D.W. (2016) Thermal structure and melting conditions in the mantle beneath the Basin and Range province from seismology and petrology. Geochemistry, Geophysics, Geosystems, 17, 1312-1338, doi:10.1002/2015GC006205.

Price, R.C., Gamble, J.A., Smith, I.E.M., Maas, R., Waight, T., Stewart, R.B., and Woodhead, J. (2012) The anatomy of an andesite volcano: A time-stratigraphic study of andesite petrogenesis and crustal evolution at Ruapehu Volcano, New Zealand. Journal of Petrology 53, 2139-2189.

Putirka, K.D. (2005) Igneous thermometers and barometers based on plagioclase + liquid equilibria: Tests of some existing models and new calibrations. American Mineralogist, 90, 336-346, doi:10.2138/am.2005.1449.

Putirka, K.D. (2008) Thermometers and barometers for volcanic systems. Reviews in Mineralogy & Geochemistry, 69, 61-120.

Putirka, K. (2016) Rates and styles of planetary cooling on Earth, Moon, Mars, and Vesta, using new models for oxygen fugacity, ferric-ferrous ratios, olivine-liquid Fe-Mg exchange, and mantle potential temperature. American Mineralogist, 101, 819-840, doi:10.2138/am-2016-5402.

Rea, J., Wallace, P.J., and Clynne, M.A. (2012) Pre-eruptive volatile contents of mafic magmas from the 2.0-1.7 ka Castle Creek eruptive period, Mount St. Helens, WA. EOS, American Geophysical Union, Fall Meeting 2012, Abstract V53C-2853.

Rees Jones, D.W., Katz, R.F., Tian, M., and Rudge, J.F. (2018) Thermal impact of magmatism in subduction zones. Earth and Planetary Science Letters, 481, 73-79, doi:10.1016/j.epsl.2017.10.015.

Reiners, P.W., Hammond, P.E., McKenna, J.M., and Duncan, R.A. (2000) Young basalts of the central Washington Cascades, flux melting of the mantle, and trace element signatures of primary arc magmas. Contributions to Mineralogy and Petrology, 138, 249-264.

Reubi, O., and Blundy, J (2009) A dearth of intermediate melts at subduction zone volcanoes and the petrogenesis of arc andesites. Nature, 461, 1269–1273, doi:10.1038/nature08510.

Reubi, O., Nicholls, I.A., and Kamenetsky, V.S. (2002) Early mixing and mingling in the evolution of basaltic magmas: Evidence from phenocryst assemblages, Slamet Volcano, Java, Indonesia. Journal of Volcanology and Geothermal Research, 119, 255-274.

Rhodes, J.M., and Dungan, M.A. (1979) The evolution of ocean-floor basaltic magmas. In M. Talwani, C.G. Harrison, and D.E. Hayes, Eds., Deep Drilling Results in the Atlantic Ocean: Oceanic Crust. American Geophysical Union, Washington, D.C., p. 262-272.

Roeder, P.L., and Emslie, R.F. (1970) Olivine–liquid equilibrium. Contributions to Mineralogy and Petrology, 29, 275–289.

Rondenay, S., Abers, G.A., and van Keken, P.E. (2008) Seismic imaging of subduction zone metamorphism. Geology, 36, 275-278.

Rowe, M.C., Kent, A.J.R., and Nielsen, R.L. (2009). Subduction influence on oxygen fugacity and trace and volatile elements in basalts across the Cascade Volcanic Arc. Journal of Petrology, 50, 61-91.

Rutherford, M.J., and Devine, J.D., III (2008) Magmatic conditions and processes in the storage zone of the 2004-2006 Mount St. Helens dacite. In D.R. Sherrod, W.E. Scott, W.E., and P.H. Stauffer, Eds., A volcano rekindled: The renewed eruption of Mount St. Helens, 2004–2006. U.S. Geological Survey Professional Paper 1750, p. 703-725.

Sakuyama, M. (1981) Petrological study of the Myoko and Kurohime volcanoes, Japan: Crystallization sequence and evidence for magma mixing. Journal of Petrology, 22, 553-583, doi:10.1093/petrology/22.4.553.

Sisson, T.W., and Layne, G.D. (2000) H_2O in basalt and basaltic andesite glass inclusions from four subduction-related volcanoes. Earth and Planetary Science Letters, 117, 619-635.

Sisson, T.W., Salters, V.J.M., and Larson, P.B. (2014) Petrogenesis of Mount Rainier andesite: Magma flux and geologic controls on the contrasting differentiation styles at stratovolcanoes of the southern Washington Cascades. Geological Society of America Bulletin, 126, 122-144, doi:10.1130/B30852.1.

Smith, D.R., and Leeman, W.P. (1987) Petrogenesis of Mount St. Helens dacitic magmas. Journal of Geophysical Research, 92, 10313-10334.

Smith, D.R., and Leeman, W.P. (1993) The origin of Mount St. Helens andesites. Journal of Volcanology and Geothermal Research, 55, 27-303, doi:10.1016/0377-0273(93)90042-P.

Smith, D.R., and Leeman, W.P. (2005) Chromian spinel-olivine phase chemistry and the origin of primitive basalts of the southern Washington Cascades. Journal of Volcanology and Geothermal Research, 140, 49-66.

Solano, J.M.S., Jackson, M.D., Sparks, R.S., and Blundy, J. (2014) Evolution of major and trace element composition during melt migration through crystalline mush:

42

Implications for chemical differentiation in the crust. American Journal of Science, 314, 895-939, doi:10.2475/05.2014.01.

Solano, J.M.S., Jackson, M.D., Sparks, R.S.J., Blundy, J.D., and Annen, C. (2012) Melt segregation in deep crustal hot zones: A mechanism for chemical differentiation, crustal assimilation and the formation of evolved magmas. Journal of Petrology, 53, 1999–2026 (2012). doi:10.1093/petrology/egs041.

Sparks, S.R.J., Sigurdsson, H., and Wilson, L. (1977) Magma mixing: A mechanism for triggering acid explosive eruptions. Nature 267, 315–318, doi:10.1038/267315a0.

Spiegelman, M., Kelemen, P.B., and Aharonov, E. (2001) Causes and consequences of flow organization during melt transport: The reaction infiltration instability in compactible media. Journal of Geophysical Research, 106, 2061–2077, doi:10.1029/2000JB900240.

Streck, M.J. (2008) Mineral textures and zoning as evidence for open system processes. Reviews in Mineralogy and Geochemistry, 69, 595-622.

Streck, M.J., and Leeman, W.P. (2018) Petrology of 'Mt. Shasta' high-magnesian andesite (HMA): A product of multi-stage crustal assembly. American Mineralogist, 103, 216-240, doi:10.2138/am-2018-6151.

Streck, M.J., Leeman, W.P., and Chesley, J. (2007) High-magnesian andesite from Mount Shasta: A product of mixing and contamination, not a primitive mantle melt. Geology, 35, 351-354, doi:10.1130/G23286A.1;3.

Streck, M.J., Broderick, C.A., Thornber, C.R., Clynne, M.A., and Pallister, J.S. (2008) Plagioclase populations and zoning in dacite of the 2004–2005 Mount St. Helens eruption: Constraints for magma origin and dynamics. In D.R. Sherrod, W.E. Scott, W.E., and P.H. Stauffer, Eds., A volcano rekindled: The renewed eruption of Mount St. Helens, 2004–2006. U.S. Geological Survey Professional Paper 1750, p. 791-808.

Streck, M.J., Dungan, M.A., Malavassi, E., Reagan, M.K., and Bussy, F. (2002) The role of basalt replenishment in the generation of basaltic andesites of the ongoing activity at Arenal volcano, Costa Rica: Evidence from clinopyroxene and spinel. Bulletin of Volcanology, 64, 316-327.

Streck, M.J., Smith, R.S., Conrey, R.M., Evarts, R.C., and Leeman, W.P. (2009) Mineralogic evidence for magma sources, mixing, and ascent of basaltic to andesitic

43

lavas of the Boring Volcanic Field (BVF), Portland Basin, Oregon. Geological Society of America Abstracts with Programs, 41, no. 7, 191.

Strong, M., and Wolff, J. (2003) Compositional variations within scoria cones. Geology, 31, 143-146, doi:10.1130/0091-7613(2003)031<0143:CVWSC>2.0.CO;2.

Sugawara, T. (2000) Empirical relationships between temperature, pressure, and MgO content in olivine and pyroxene saturated liquid. Journal of Geophysical Research, 105, 8457-8472.

Sun, S.-S., and McDonough, W.F. (1989) Chemical and isotopic systematics of oceanic basalts; implications for mantle composition and processes. In A.D. Saunders, and M.J. Norry, Eds., Magmatism in the ocean basins. Geological Society of London Special Publications 42, p. 313-345.

Syracuse, E.M., van Keken, P.E. and Abers, G.A. (2010) The global range of subduction zone thermal models. Physics of the Earth and Planetary Interiors, 183, 73-90.

Tamura, Y., Tatsumi, Y., Zhao, D., Kido, Y., and Shukuno, H. (2002) Hot fingers in the mantle wedge; new insights into magma genesis in subduction zones. Earth and Planetary Science Letters, 197, 105-116.

Thomson, A., and Maclennan, J. (2013) The distribution of olivine compositions in Icelandic basalts and picrites. Journal of Petrology, 54, 745-768, doi:10.1093/petrology/egs083.

van Keken, P.E., Hacker, B.R., Syracuse, E.M. and Abers, G.A. (2011) Subduction factory: 4. Depth-dependent flux of H_2O from subducting slabs worldwide. Journal of Geophysical Research, 116: B01401, doi:10.1029/2010JB007922.

Wackett, A., and Smith, D.R. (2013) Microanalytical evidence for magma mingling at Mount St. Helens. Geological Society of America Abstracts with Programs, 45, no. 7, 590.

Wanke, M., Bachmann, O., Ellis, B.S., Guillong, M., Clynne, M.A., and Pallister, J.S. (2016) Insights into the Mount St. Helens magma plumbing system from coarse-grained, crystal-rich enclaves. EOS, American Geophysical Union, Fall Meeting, Abstract V33B-3127.

44

Waters, L.E., and Lange, R.A. (2015) An updated calibration of the plagioclase-liquid hygrometer-thermometer applicable to basalts through rhyolites. American Mineralogist, 100, 2172-2184.

Wells, R.E., Blakely, R.J., Wech, A.G., McCrory, P.A., and Michael, A. (2017) Cascadia subduction tremor muted by crustal faults. Geology, 45, 515-518, doi:10.1130/G38835.1

Williams, D.A., Kadel, S.D., Greeley, R., Lesher, C.M., and Clynne, M.A. (2004) Erosion by flowing lava: Geochemical evidence in the Cave Basalt, Mount St. Helens, Washington. Bulletin of Volcanology, 66, 168-181.

Zellmer, G.F., Pistone, M., Iizuka, Y., Andrews, B.J., Gómez-Tuena, A., Straub, S.M., and Cottrell, E. (2016) Petrogenesis of antecryst-bearing basalts from the Trans-Mexican Volcanic Belt: Insights into along-arc variations in magma-mush ponding depths, H_2O contents, and surface heat flux. American Mineralogist, 101, 2405-2422, doi:10.2138/am-2016-5701.

FIGURE CAPTIONS

Figure 1. Locations of samples considered in this study shown on base map modified after the Cougar and Mount St. Helens 15° quadrangles published by the USGS in 1953 and 1958, respectively, which show the pre-1980 configuration of the volcano. Orange shaded fields show the extent of the Cave Basalt (Greeley and Hyde, 1972; Hopson, 2008). Latitude-longitude positions are keyed to map location numbers in Table 1. Where vertical stratigraphic sequences were sampled (locations *Nfa* and *Nfb*), the number of samples collected is given in parentheses. The inset (after Hildreth, 2007) in upper left shows the locations (filled triangles) of Mounts St. Helens (MSH), Rainier (R), Adams (A) and Hood (H). Portland Basin (PB) and Indian Heaven (IH) volcanic fields are indicated by dash outlines and Battleground (BG) is shown by small dark gray oval.

Figure 2. Major element oxides plotted against wt% MgO for samples from MSH and representative samples of primitive basalts of the CCT (data are from Smith and Leeman, 1987, 1993; Leeman et al., 1990, 2004, 2005; this paper). Legend shows symbols for Castle Creek Group A lavas (of LKT affinity; squares) and Group B lavas (of IPB affinity; circles). Symbols for Group B lavas distinguish between nepheline-normative basalts from location *Nfa* (Group B1), hypersthene-normative basalts from location *Nfb*, and all other hypersthene-normative basalts (Group B2); see text for further explanation. Also shown are a Castle Creek andesite (gray diamond), Kalama age andesite (open diamond), and MSH andesites and dacites of all ages (yellow diamonds and grey triangles, respectively). Representative primitive basalts from the CCT include LKTs (blue asterisks), ne-normative IPBs (black crosses), and hy-normative IPBs (orange crosses). Fields are drawn around MSH andesites and dacites and primitive CCT groups.

Figure 3. Selected trace elements plotted against wt% MgO for samples from MSH and the CCT. Symbols and fields as in Figure 2.

Figure 4. K_2O and FeO*/MgO vs. SiO_2 diagram for MSH and primitive CCT lavas. The blue line is the boundary between tholeitiic vs. calcalkalic compositions as defined by Miyashiro (1974). Symbols as in Figure 2.

Figure 5. Representative MSH basalts normalized to primitive mantle. Normalizing values from Sun and McDonough (1989). The same MSH basalts are compared in successive frames with similarly-normalized data for primitive IPBs (blue), CABs (green), and LKTs (gray) from the CCT; fields for the latter basalt types are based on compilations of Evarts et al. (2017), and averages are presented in Supplement Table A2.

Figure 6. Olivine crystal size vs. core compositions. This diagram illustrates the diverse populations of olivine 'macrocrysts' in MSH basaltic lavas.

Figure 7. Rhodes diagram for Kalama andesite DS-79, illustrating olivine vs. whole-rock Mg#s (calculated with $X_{Fe}^{3+} = 0.15$). Gray field and dashed curves illustrate the olivine-liquid equilibrium band for $K_D^{Mg/Fe} = 0.30 \pm 0.3$. Olivine core compositions and representative BSE images are shown. Olivines that lie above the equilibrium band (e.g., red diamond) can be explained by inheritance from more magnesian liquids, whereas olivines below the band (blue diamonds) likely grew from less magnesian liquids (Mg# ~45 to 30). Numbers on photographs are Fo values for olivine (black) and Mg#s for orthopyroxene (yellow). Red and green outlined scale bars represent 100 and 50 microns, respectively.

Figure 8. Rhodes diagram for Group A basalts. Olivines in these lavas are generally euhedral to equant with uniform cores and thin, normally zoned rims. They commonly form glomeroporphyritic clusters with plagioclase. Except for DS-27, maximum core compositions are near equilibrium. Fo_{75-70} olivines correspond to typical MSH andesite whole-rock compositions (Mg# = ~43-47).

Figure 9. Rhodes diagram for Group B lavas from location *Nfb*. Olivine macrocrysts in these samples show large ranges in core Fo contents. Some olivines appear to be in equilibrium with the whole-rock composition, but other grains are likely derived from more primitive magmas. The *least* evolved *Nfb* sample (DS-72) has olivine grains with core compositions (down to Fo_{64}) lower than predicted from the whole-rock Mg#. Those latter grains exhibit evidence of disequilibrium including embayments and reverse zoning. DS-74 is the *most* evolved IPB sample (Mg# = 52) from this locality; see Figure 12 for additional images of this sample.

47

Figure 10. Rhodes diagrams for Group B lavas from location *Nfa* and south flank locations. Olivine grains in most samples from location *Nfa* exhibit fairly limited ranges of core compositions, generally <10 mol% Fo, and tend to be euhedral or equant with thin, normally zoned rims. Grains with Fo_{72-70} in the most evolved sample (DS-9) suggest input from more evolved magma. The *least* evolved sample (DS-4) exhibits petrographic evidence for magma mixing (see Figure 11 for details). Both samples PB-29 and PB-28 from the south flank exhibit relatively large ranges in mol% Fo (85-67 and 86-74, respectively); resorbed and/or skeletal grains with Fo_{76} were found in both samples.

Figure 11. Photomicrographs of DS-4 under crossed (Panel A) and uncrossed (Panel B) polars. This sample has the highest whole-rock Mg# among *Nfa* samples. Panel A shows glassy "globules" (outlined in white) in an intersertal to holocrystalline matrix. Fo contents in olivines within the globules overlap with those in the matrix. Panel C magnifies a "brown glassy bleb" (outlined in pink) that includes microphenocrysts of orthopyroxene (OPX; Mg# = 64-65, in yellow font) and small patches of brown silicic glass (SiO_2 = 73-75 wt%; white spots). Yellow scale bar = 1 mm.

Figure 12. BSE images and SEM analyses of olivine occurring in Group B sample DS-74. These olivine grains span a wide range of core compositions, from Fo_{81} to Fo_{58}. Those with mol% Fo >70 exhibit normally zoned rims (e.g., Fo_{66-61}), and some exhibit thin OPX rims (Mg# = 64-66; yellow font). Note the change in olivine morphology, from euhedral to subhedral to anhedral and/or highly embayed with decreasing core Fo. In addition, OPX rims become wider as %Fo decreases.

Figure 13. MgO vs. K_2O variation diagram for MSH Castle Creek lavas and primitive basalts from the CCT. Note that symbols for Group B samples have been colored to more clearly distinguish among the subtypes (B1, B2-north, B2-south). Other symbols and fields as in Figure 2. Simple binary mixing lines (labeled M1, M2, and M3) connect average MSH andesite (yellow star) with averages for primitive CCT basalts: LKT (gray star), ne-IPB (blue star), and hy-IPB (white star). Tick marks are at 10% increments. A similar vector is shown connecting average

regional ne-IPB and LKT, but multi-element data preclude this as a viable mixing scenario (see text). Labeled curves depict simple fractional crystallization paths involving removal of olivine and plagioclase in proportions of 0.3:0.7 (FC1a and FC2) or 0.9:0.1 (FC1b) from presumed parental liquids (see text and Supplement Note 3 and Table A3 for details; plots for additional elements are provided in this table).

Figure 14. Plots showing relations between wt% SiO_2 vs. calculated [A] density, [C] temperature, [E] wt% H_2O and [G] X-andesite (fraction of assumed end member andesite). Panels [B], [D] and [F] show temperature, density, and wt% SiO_2, respectively, vs. depth. Pink boxes and yellow stars give ranges for primitive CCT basalts and average MSH andesite, respectively. MSH dacite compositions and parameters are off-scale for most of these plots; values for average MSH dacite are: SiO_2 = 64.4 wt%; depths = 7-15 km; T = 1033°C; density = 2.4 gm/cm^3. Dacite water contents are uncertain, but likely are in the range of 3-6 wt%. Typical uncertainties on the plotted parameters are as follows: SiO_2, ± 0.3 wt% ($\leq$ symbol size); depth, ± 2 km; T, ± 10°C; density, ± 0.05 kg/m^3; H_2O, ± 0.5 wt% (based on reproducibility of experimental data). Curves in [E] labeled A-FC and B-FC represent changes in water content resulting from fractional crystallization assuming 'Group A' and 'Group B' parental magmas, respectively. Tick marks represent 5% intervals of crystallization. See text and Supplement Note 5 and Table A5 for further details.

Figure 15. Left panel: Cross-section of the Cascadia subduction zone illustrating segregation P-T relations for primitive CCT lavas (cf. Leeman et al., 2005; Supplement Note 7 and Table A6). Right panel: Schematic cross-section showing inferred depth relations for MSH magma reservoirs and plumbing system as described in the text.

Figure 16. K_2O vs. MgO in eruptive products from Mt. Hood, Mt. Adams-Indian Heaven, and Simcoe volcanic fields within the CCT (ca. 46° N latitude). Green, blue, and purple arrows show generalized basalt arrays towards ne-IPB/SHO, IPB, and LKT compositions, respectively. Note the pronounced divergence of K_2O

values with increasing MgO. Red arrows represent trends for MSH basalts, which converge towards andesitic compositions (~5 wt% MgO and ~1% wt% K_2O). Data from R. Conrey (personal communication, 2005), Leeman et al. (1990, 2005), Bacon et al. (1997), Conrey et al. (1997), Hildreth and Fierstein (1997), Jicha et al. (2009) and Leeman (unpublished data).

SUPPLEMENT FIGURES

Cited Supplement figures are included in the Supplement Notes. Additional figures are also presented in the Excel files of Appendix Tables A3-A6.

TEXT TABLES

(uploaded separately)

Text Table 1. Analyses of Mount St. Helens and representative regional lavas

Text Table 2. Analyses of olivine (ol) cores and orthopyroxene (opx) rims in MSH lavas

SUPPLEMENT TABLES

All Supplement tables are uploaded as separate pages (sheets) in a single Excel file. They are listed below with titles. Note that several of these Tables (#s A3, A4, A5, A6) contain additional figures that complement those in the main text.

Supplement Table A1. Isotopic analyses of Mount St. Helens samples

Supplement Table A2. Averages for distinct variants of lavas in the CCT region and at MSH - used as 'end members' for calculations and diagrams

Supplement Table A3. Fractional crystallization models

Supplement Table A4. Estimated mixing proportions for MSH mafic lavas

Supplement Table A5. P-T-H_2O calculations for MSH lavas

Supplement Table A6. Results of olivine addition to primitive lavas and estimated segregation P and T

Table 1. Analyses of Mount St. Helens and representative regional lavas

Sample	Unit/area [a]	Map Location	Lat (°N)	Long (°W)	Elev (ft)	SiO2 [b]	TiO2	Al2O3	FeO*
MSH Group A (S Flank)									
DS-27	ccbc	1	46.056	122.247	1853	50.35	1.47	17.28	9.81
PB-32	ccbc	2	46.060	122.261	1837	50.35	1.47	17.28	9.81
PB-7	ccbc	3	46.110	122.356	1345	50.60	1.48	17.23	9.93
CB-1	ccbc	4	46.060	122.254	1200	49.81	1.49	17.44	10.29
CB-2	ccbc	5	46.095	122.215	1820	50.03	1.53	17.18	10.50
CB-3	ccbc	6	46.107	122.210	2090	49.72	1.49	17.34	10.29
CB-4	ccbc	7	46.111	122.210	2460	49.84	1.51	17.32	10.43
SL-9a	ccbc [f]	8	46.093	122.218	1680	50.53	1.48	17.28	10.68
SL-9b	ccbc [f]	8	46.093	122.218	1680	49.98	1.68	16.49	11.14
SR-15a	ccbc [f]	9	46.132	122.219	2640	50.07	1.68	16.49	11.05
SR-15b	ccbc f	9	46.132	122.219	2640	50.36	1.49	17.29	10.32
LFV	ccbc	-	-	-	-	50.05	1.52	17.67	9.98
GH1	ccbc	10	46.148	122.238	3250	50.41	1.66	16.82	10.28
GH2	ccbc	11	46.058	122.243	1810	50.34	1.46	17.21	10.04
GH3	ccbc	12	46.137	122.325	1940	49.76	1.61	17.53	10.49
L82-56	ccbpc	13	46.142	122.222	2980	51.28	1.55	17.46	9.50
PB-30	ccbpc	14	46.131	122.175	2510	52.23	1.67	17.01	9.35
MSH Group B									
SHH-17	B1: ccb-Nfa	15	46.210	122.167	6100	49.97	1.95	16.98	9.37
DS-4	B1: ccb-Nfa	16	46.221	122.167	4805	51.82	1.73	17.76	8.45
DS-5	B1: ccb-Nfa	16	46.221	122.167	4760	49.40	2.00	16.92	10.04
DS-6	B1: ccb-Nfa	16	46.221	122.167	4720	50.02	2.05	16.86	10.04
DS-7	B1: ccb-Nfa	16	46.221	122.167	4690	50.07	1.99	16.30	10.45
DS-9	B1: ccb-Nfa	16	46.221	122.167	4750	49.05	2.11	16.71	11.04
L01-17	B2: ccb-Nfc	17	46.211	122.249	3600	51.82	1.76	16.93	9.15
DS-71	B2: ccb-Nfb	18	46.229	122.187	4540	52.18	1.23	18.36	9.44
DS-72	B2: ccb-Nfb	18	46.229	122.187	4540	53.05	1.43	18.36	8.15
DS-74	B2: ccb-Nfb	18	46.229	122.187	4590	53.72	1.30	18.72	8.65
DS-76	B2: ccb-Nfb	18	46.229	122.187	4590	52.50	1.40	18.25	9.33
DS-77	B2: ccb-Nfb	18	46.229	122.187	4590	51.04	1.56	17.68	9.96
DS-78	B2: ccb-Nfb	18	46.229	122.187	4590	52.25	1.54	17.32	9.58
L82-63	B2: ccb-Sf	19	46.137	122.239	3500	51.48	1.84	17.21	8.92
PB-28	B2: ccb-Sf	20	46.143	122.225	2950	54.66	1.51	16.86	8.54
GH5	B2: ccb-Sf	21	46.144	122.213	3120	54.22	1.51	16.77	8.87
PB-29*	B2: ccb-Sf	22	46.144	122.202	3160	53.50	1.59	16.47	8.89
L82-40*	B2: ccb-Sf	22	46.144	122.203	3200	53.67	1.62	16.56	8.90

L82-41A*	B2: ccb-Sf	22	46.144	122.203	3220	53.69	1.62	16.66	8.90
%CV for unit (3 *samples) [g]						0.20%	0.92%	0.58%	0.09%

Andesites

L82-55	CC andesite-Sf	23	46.145	122.215		56.60	1.24	17.46	6.95
DS-79	Kalama andesite	24	46.170	122.216		56.56	1.18	17.43	7.57

Representative primitive CCT lavas for which olivine data are available in this study

DS-80A-80	IH, Ice Cave	LKT[h]	45.879	121.518		48.30	1.16	17.51	10.98
DS-6A-80	IH, S. Prairie	hy-IPB	45.914	121.699		50.58	1.14	17.30	9.51
DS-49A-80	IH, Flattop Mt.	ne-IPB	46.023	121.595		49.53	1.95	16.40	9.39
PB-9	FA, Battleground	ne-IPB	45.825	122.443		49.42	2.00	16.53	9.27
DS-42-81	IH, Deep Lake	SHO	46.037	121.766		52.66	1.13	16.04	7.36

[a] Unit designations: ccbc, Cave basalt; ccbpc, pre-Cave basalt; ccb, Castle Creek basalt: Nfa=NE flank,

[b] Major element oxides normalized to 100% with all Fe as FeO*

[c] Mg# = molar Mg/(Mg+Fe2+)*100, with X-fe3 = 0.15

[d] Calculated equilibrium olivine as mol% Fo, assuming $K_D = 0.3$

[e] Data sources: 1. Greeley & Hyde (1972); 2. Lopez-Escobar et al. (1977); 3. Halliday et al., (1983);

[f] Sample from lava tube inner lining

[g] Percent coefficient of variation for three samples of the same unit

[h] Magma types: Low-K Tholeiite (LKT), hypersthene- or nepheline-normative Intraplate Basalt (hy- or

Additional notes:

1. It is apparent to us that major element data originally reported for our sample DS-27 (Leeman et al
Thus, another sample (PB-32) from a nearby location was analyzed by higher precision XRF. In
substituted for older data for DS-27. The trace element data for DS-27 were verified by ICP-MS

2. Regarding representativeness of the data, note that three of our samples (L82-40, L82-41A, a
RSDs given for these data in Table 1 are comparable to reproducibility of repeat analyses on ind

3. Additional analyses are available for four samples (SL- and SR- prefixes) of lava tube linings
Trace element data for these samples are consistent with data reported by same authors for Cav
albeit slightly enriched in incompatible elements owing to concentration of interstitial liquid segre

MnO	MgO	CaO	Na2O	K2O	P2O5	FeO/MgO	Mg# [c]	Calc Fo [d]	Ba	Rb	Sr
0.16	6.87	9.89	3.49	0.50	0.18	1.43	59.5	83.0	113	9.6	315
0.16	6.87	9.89	3.49	0.50	0.18	1.43	59.5	83.0	123	9.1	337
0.16	6.70	9.91	3.24	0.55	0.20	1.48	58.6	82.5	154	13.1	335
0.17	6.92	9.70	3.50	0.51	0.17	1.49	58.5	82.5		9.4	346
0.17	6.88	9.52	3.48	0.54	0.17	1.53	57.9	82.1		10	343
0.17	7.02	9.76	3.54	0.50	0.16	1.47	58.8	82.7		9.3	342
0.16	6.90	9.71	3.46	0.50	0.17	1.51	58.1	82.2		9.7	354
0.17	6.35	9.17	3.62	0.56	0.17	1.68	55.5	80.6		11.6	361
0.18	6.75	9.52	3.52	0.54	0.18	1.65	55.9	80.9		10.8	341
0.18	6.54	9.59	3.66	0.56	0.18	1.69	55.4	80.6		11.4	344
0.17	6.71	9.42	3.53	0.54	0.17	1.54	57.7	82.0		10.8	356
0.17	6.79	9.87	3.33	0.48	0.14	1.47	58.8	82.6	135		380
0.15	7.14	9.47	3.33	0.49	0.24	1.44	59.3	82.9			
0.14	6.99	9.73	3.38	0.50	0.21	1.44	59.3	83.0			
0.15	6.64	9.72	3.41	0.52	0.16	1.58	57.1	81.6			
0.15	6.18	9.39	3.62	0.65	0.20	1.54	57.7	82.0		15	363
0.16	5.58	9.24	3.72	0.80	0.26	1.68	55.6	80.7	210	15.8	387
0.15	7.00	9.01	3.89	1.28	0.40	1.34	61.0	83.9	309	20	577
0.13	6.20	8.31	4.24	1.17	0.20	1.36	60.6	83.7	275	25	581
0.14	7.18	8.72	3.90	1.26	0.44	1.40	60.0	83.3	272	27	589
0.15	6.63	8.64	3.89	1.31	0.41	1.52	58.0	82.2	307	23.3	608
0.15	6.85	8.56	3.91	1.34	0.38	1.53	57.9	82.1	319	27	577
0.15	6.69	8.73	3.79	1.36	0.37	1.65	56.0	79.7	312	24	590
0.14	6.57	8.39	3.87	1.00	0.36	1.39	60.1	83.4	259	18.2	513
0.13	5.21	8.00	4.26	0.95	0.25	1.81	53.6	79.4	216	19	511
0.13	5.47	7.97	4.27	0.99	0.17	1.49	58.4	82.4	225	23	528
0.12	4.46	7.38	4.42	1.04	0.19	1.94	52.0	78.3	244	25	518
0.13	5.16	7.72	4.28	1.02	0.20	1.81	53.7	79.5	226	25	527
0.13	6.18	8.00	4.22	0.97	0.25	1.61	56.5	81.3	221		493
0.13	5.89	7.95	4.04	1.00	0.29	1.63	56.3	81.1	262	21	514
0.14	6.79	8.39	3.81	1.09	0.33	1.31	61.5	84.2		20	574
0.14	5.14	7.87	3.99	1.03	0.26	1.66	55.8	80.8	239	23.2	465
0.13	5.40	7.78	3.93	1.06	0.32	1.64	56.1	81.0			
0.14	6.25	7.87	3.92	1.04	0.33	1.42	59.6	83.1	281	20.7	485
0.14	6.14	7.69	3.90	1.05	0.32	1.45	59.1	82.8		22	476

0.15	6.05	7.72	3.86	1.04	0.30	1.47	58.8	82.6		22	468
3.70%	*1.64%*	*1.29%*	*0.71%*	*0.41%*	*3.80%*	*1.70%*	*0.70%*	*0.29%*	*na*	*3.48%*	*1.76%*
0.11	4.86	7.18	4.17	1.21	0.21	1.43	59.5	83.0		24.0	594
0.11	4.24	6.89	4.43	1.24	0.35	1.78	54.0	79.7	333	28.0	595
0.18	8.37	9.89	3.23	0.22	0.16	1.31	61.5	84.2	63	2.5	259
0.16	8.21	9.34	3.15	0.39	0.22	1.159	64.4	85.8	98	9	291
0.16	8.46	8.98	3.47	1.24	0.43	1.110	65.4	86.2	327		688
0.15	8.03	9.37	3.29	1.41	0.54	1.154	64.5	85.8	372	16.0	914
0.12	8.41	8.49	3.62	1.74	0.43	0.874	70.6	88.9	563	21.5	1058

Nfb = N flank, Nfc = NW flank, Sf = south flank; Group B is subdivided into distinct B1 and B2 sub-groups

4. Leeman et al. (1990); 5. Smith & Leeman (1993); 6. Williams et al. (2004); **7. This paper**

ne-IPB), Shoshonite (SHO)

l., 1990) were anomalous.
Table 1 the major element data for PB-32 are
5 and these data are reported in Table 1.

and PB-29) represent the same eruptive unit;
ividual samples.

from Cave basalt (Williams et al., 2004).
e basalt surface samples (CB- prefixes),
egated from this porphyritic lava flow.

Y	Zr	Nb	V	Ni	Cr	Sc	La	Yb	Lu	Hf	Ta
22.2	132	7.82	210	85	175	33.3	7.0	2.11	0.33	2.78	0.46
25.1	117	8.20	205	85	160	33	8.0	*2.11*	*0.33*	*2.78*	*0.46*
22.0	143	10.0	229	76	164	36	10.6	2.49	0.38	2.98	0.59
25.6	110	7.58					8.63	2.38	0.37	3.08	0.39
25.1	110	7.71					8.89	2.40	0.36	3.20	0.40
24.7	109	7.57					8.27	2.33	0.36	3.03	0.38
25.0	110	7.82					8.60	2.27	0.37	3.12	0.38
24.3	112	7.78					8.95	2.30	2.30	3.07	0.39
29.2	120	8.26					9.32	2.60	0.40	3.31	0.42
28.6	121	8.36					9.9	2.56	0.40	3.31	0.49
25.1	109	7.72					9.1	2.27	0.37	3.01	0.42
				80	170	34	8.9	1.91	0.41		
27.0	139	11		64	140	31	10.2	2.41	0.38	3.20	0.56
27.9	151	10.4	213	60	134	32	13.1	2.50	0.38	3.54	0.51
24.0	174	22	230	82	159	28.2	22.6	2.40	0.36	4.70	
17.5	188	21.8	188	80	169	24.6	10.8	1.69	0.25	4.10	1.41
	207		219	86	196	25.5	22.7	2.20	0.32	4.30	2.30
23.9	203	32.7	212	97	196	25.9	21.9	1.98	0.31	4.58	2.08
	203		211	81	157	27.3	19.8	2.08	0.33	4.40	2.07
26.2	200	28.5	214	84	155	28.5	19.8	2.20	0.30	4.50	2.13
24.0	157	21.2	190	95	180	23	18.0	2.22	0.31	3.88	1.28
	156		178	58	98	21.9	10.0	1.68	0.25	3.60	0.80
21.3	154	12.5	184	66	113	19.1	11.3	1.61	0.25	3.10	0.67
	153		174	57	63	19	10.5	1.68	0.24	3.50	0.66
	165		179	61	99	21.8	10.9	1.70	0.24	3.60	0.80
	170		188	72	137						
	178		187	76	152	23.9	14.3	2.10	0.31	3.90	0.96
21	176	24.0		103							
24.9	156	12.0	172	65	118	25	14.2	2.22	0.33	3.52	0.67
25.3	170	18.1	172	111	182	24	17.8	2.25	0.33	3.78	0.97
28	181	18.0		107							

26	178	18.0		104	175	23.4	15.6	2.23	0.34	4.20	0.95
5.30%	*3.26%*	*0.32%*	*na*	*3.32%*	*2.77%*	*0.60%*	*9.32%*	*0.63%*	*1.90%*	*7.44%*	*1.62%*
16.0	162	17.0		49	96	19	12.4	1.46	0.23	3.70	0.86
19.6	173	17.5	148	40	92						
18.8	75	3.8	187	110	208	29.1	4.0	1.81	0.29	1.85	0.26
20.7	99		165	108	280	28.5	7.2	2.02	0.33	2.60	0.37
20.9	183		213	170	313	24.8					
21.0	196	31.5	198	130	227	26	30.2	1.95	0.28	4.44	1.46
14.7	184	7.9	169	183	334	20.1	40	1.50	0.22	4.84	0.54

Th	Data Source [e]
0.74	4, 7
0.74	7
1.18	7
0.90	6
0.92	6
0.86	6
0.91	6
1.03	6
0.99	6
1.04	6
0.97	6
	2
	1
	1
	1
1.40	4
1.52	7
3.10	3
2.05	4
2.60	5
2.21	5
2.22	5
2.26	4
2.14	7
1.54	5
1.36	5
1.64	5
1.66	5
	5
1.84	5
	5
1.85	7
	1
2.04	7
	5

2.10   5

2.05%

2.40   7
           7

0.48   4
0.84   7
           7
3.15   7
6.85   7

Table 2. Analyses of olivine (ol) cores and orthopyroxene (opx) rim

	Group A				Group B1		
	DS-27	PB-32	PB-28	PB-30	*Nfa* DS-4	*Nfa* DS-7	
WR Mg# (0.85) [a]	59.5	59.5	55.8	55.6	60.6	57.9	
WR SiO$_2$ [b]	50.35	50.35	54.66	52.23	51.8	50.07	
Source [c]	MSH	MSH	MSH	MSH	MSH	MSH	
Calculated forsterite contents [d]							
	81.9	81.9	80.1	79.8	82.8	80.8	
					SEM	***EMP***	
Mineral	*ol*	*ol*	*ol*	*ol*	*ol*	*ol*	*ol*
# spots	15	34	23	14	27	18	25
# phenocrysts	14	15	16	11	13	18	22
Measured forsterite contents:							
Maximum	77	82	86	79	85	85	85
Minimum	72	71	74	73	78	77	80
Average	76	76	77	76	82	81	83
SD	1	3	3	2	3	3	1

Footnotes:

[a] WR Mg# (0.85) = Whole rock Mg# assuming Fe2+/∑Fe = 0.85 (see Tabl

[b] WR SiO$_2$ = Whole rock wt% SiO2 (see Table 1)

[c] Source: MSH = Mount St. Helens; IH = Indian Heaven; FA = Frontal Arc

[d] Equilibrium forsterite contents calculated using the WR Mg# given above

[e] EMP analyses by Carroll (2009) extend the compositional range for olivin
All data are by SEM-EDS analysis, with exception of EMP data denoted fo

ηs in MSH lavas

	Group B2							
Nfa	*Nfb*	*Nfb*	*Nfb*	*Nfb*	*Nfb*		*Nfc*	*Sf*
DS-9	DS-72	DS-77	DS-78	DS-71	DS-74		L01-17 [e]	PB-29
56.0	58.4	56.5	56.3	53.6	52.0		60.1	59.6
49.05	53.05	51.04	52.25	52.18	53.72		51.82	53.50
MSH	MSH	MSH	MSH	MSH	MSH		MSH	MSH
79.7	81.8	80.2	80.2	78.7	77.9		82.3	82.1
							EMP	
ol	*ol*	*ol*	*ol*	*ol*	*ol*	*opx*	*ol*	*ol*
26	60	35	32	23	27	16	16	45
15	43	29	24	14	22	13	NA	24
84	84	84	85	83	81	68	84	85
71	64	64	74	60	58	63	77	68
80	78	77	80	77	74	65	81	78
3	5	5	3	6	6	1	2	4

le 1)

ᶜ (Battleground)
 and K_D = 0.30 (Roeder and Emslie, 1970)
es in this sample to Fo_{72}
r samples DS-4 and L01-17.

Kalama andesite		Primitive Cascades (CCT) basaltic lavas				
DS-79		DS-80A-80 LKT	DS-6A-80 hy-IPB	DS-49A-80 ne-IPB	PB-9 ne-IPB	DS-42-81 SHO
54.0		61.5	64.4	65.4	64.5	70.6
56.00		48.30	50.58	49.53	49.42	52.66
MSH		IH	IH	IH	FA	IH
79.7		84.2	85.8	86.2	85.8	88.9
ol	*opx*	*ol*	*ol*	*ol*	*ol*	*ol*
27	9	23	32	22	37	34
16	6	20	26	18	17	21
83	70	82	85	86	86	89
61	66	75	76	65	79	78
69	68	78	82	79	83	86
7	1	2	3	5	2	3
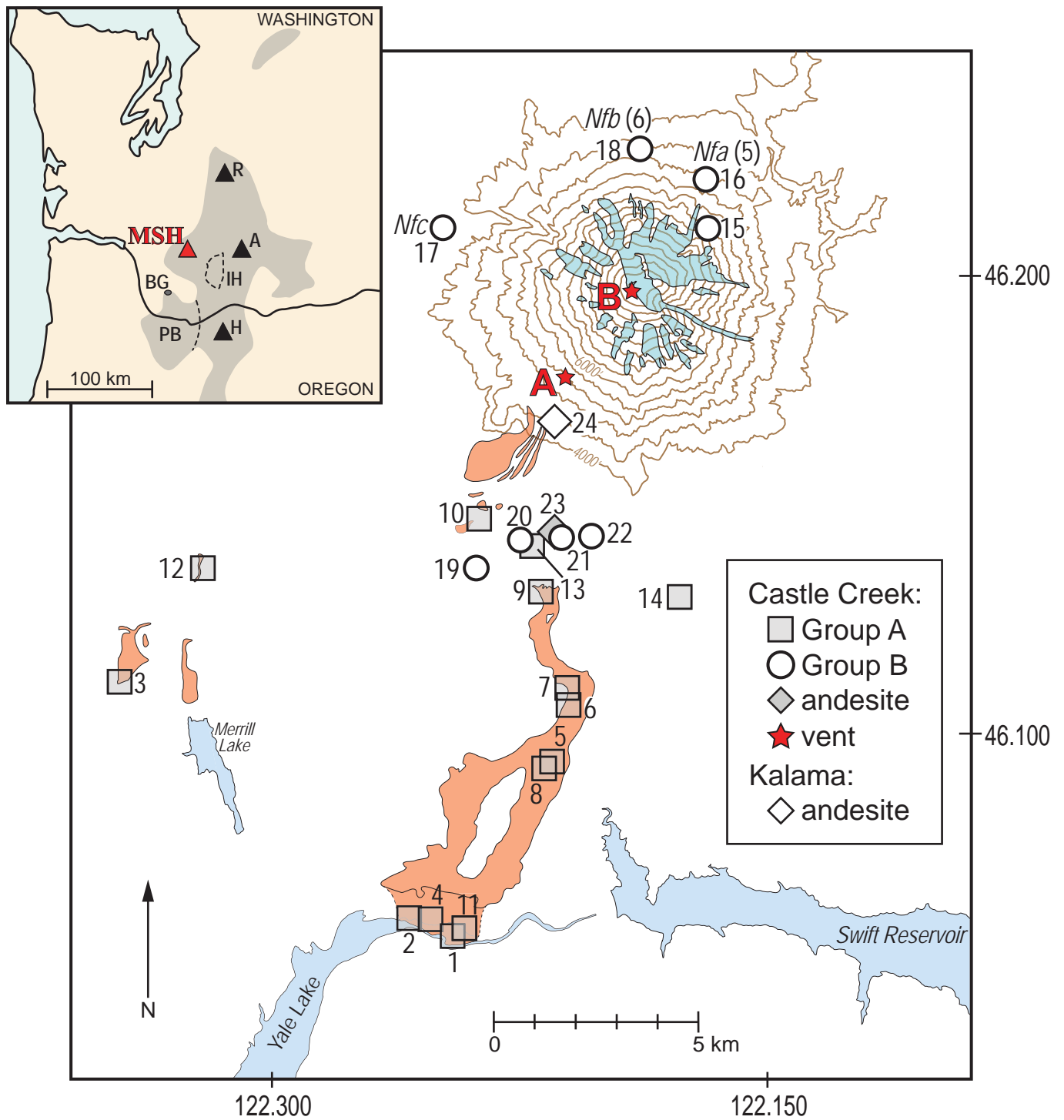
FIGURE 1.
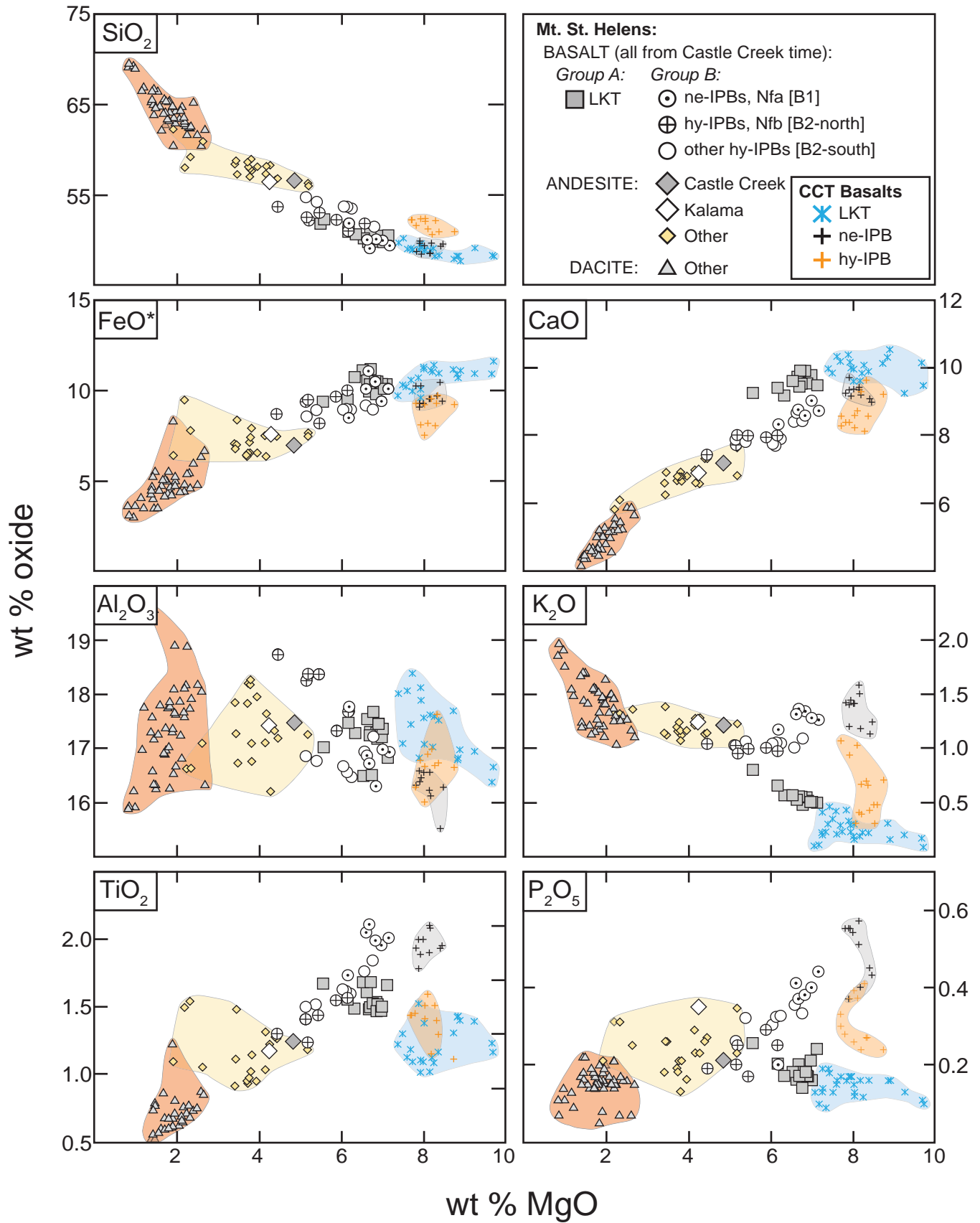
Figure 2.
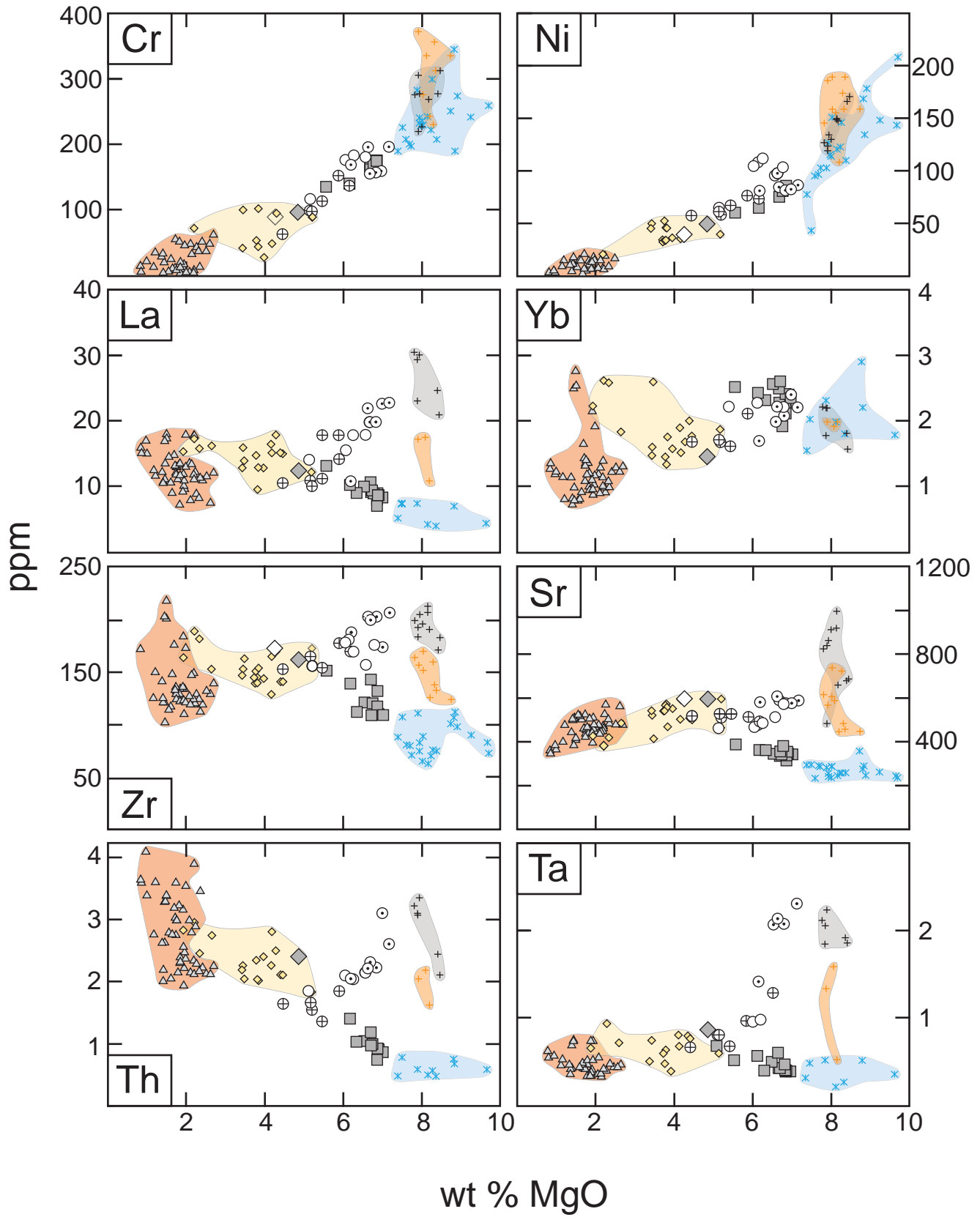
Figure 3.
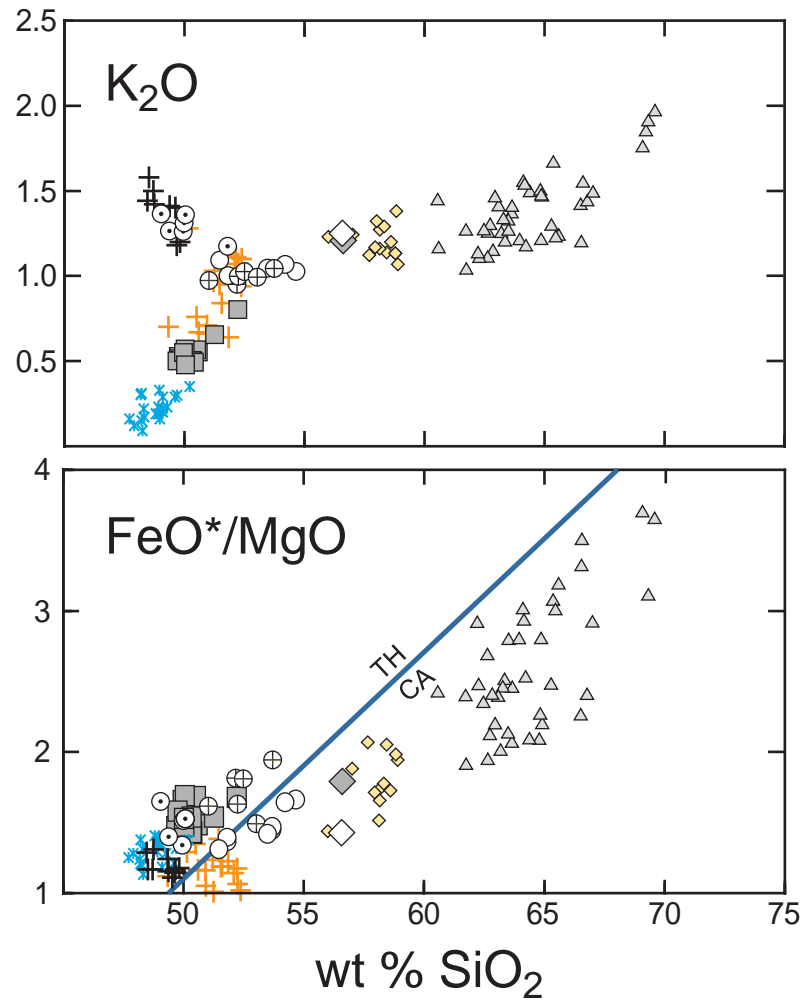
Figure 4.
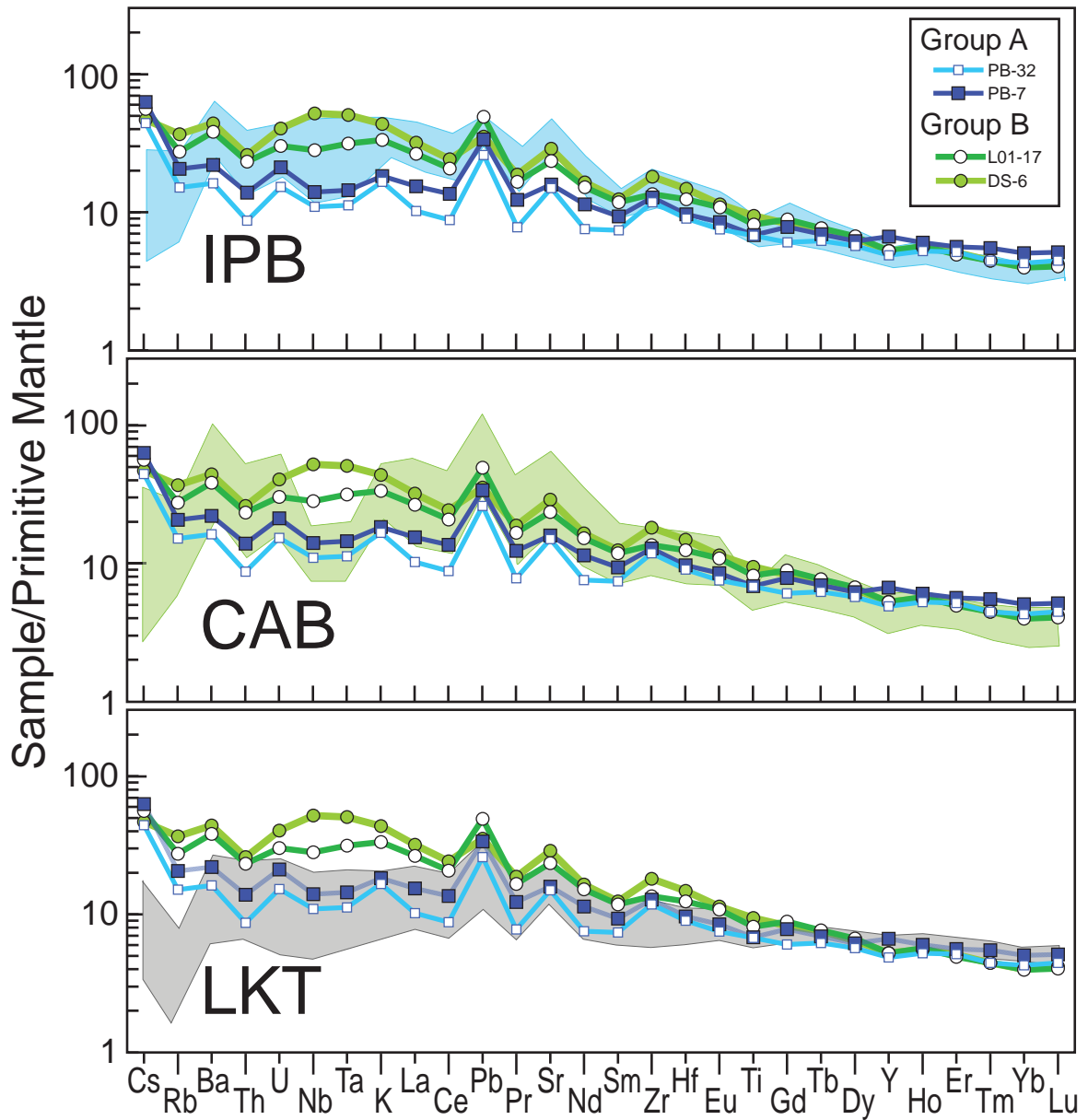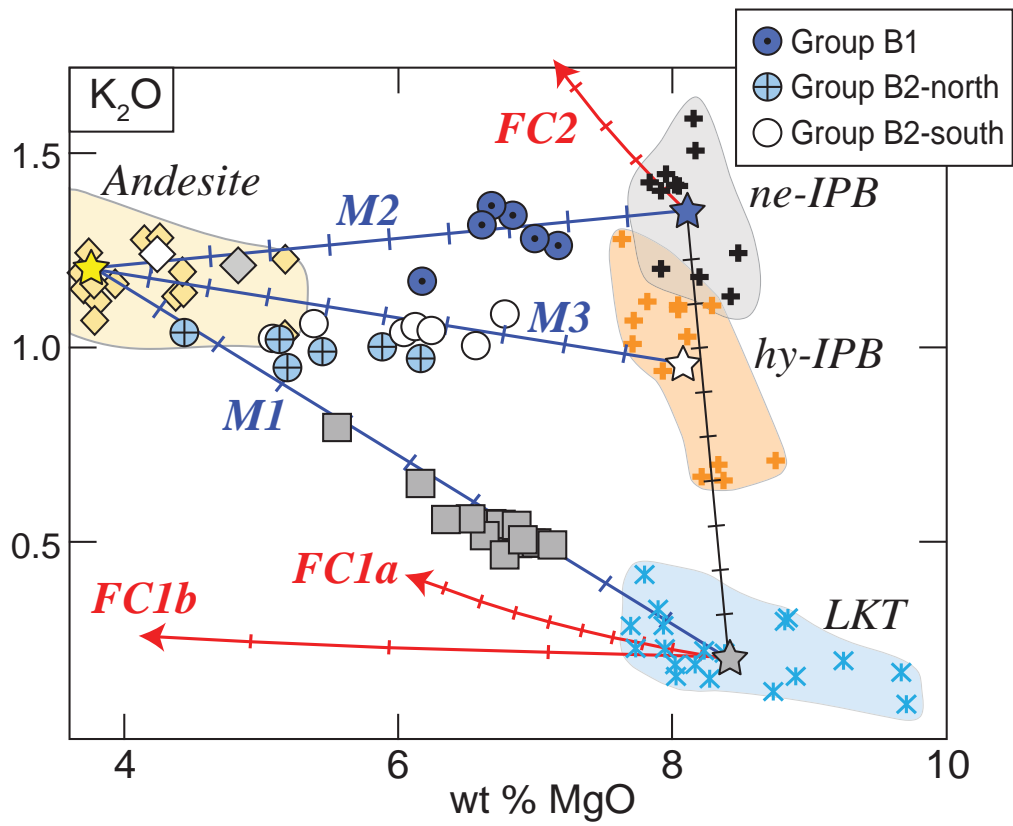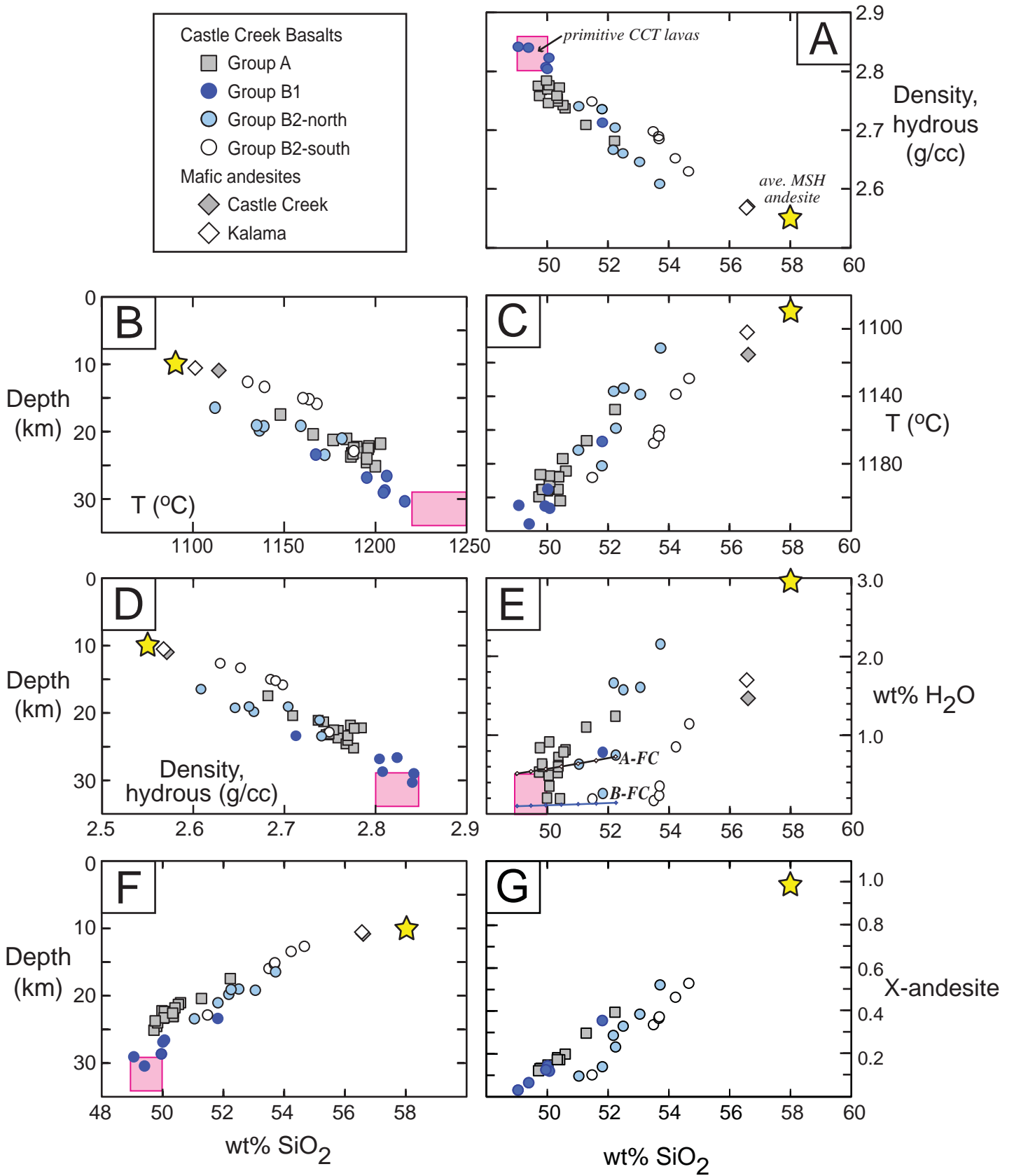
Figure 5.
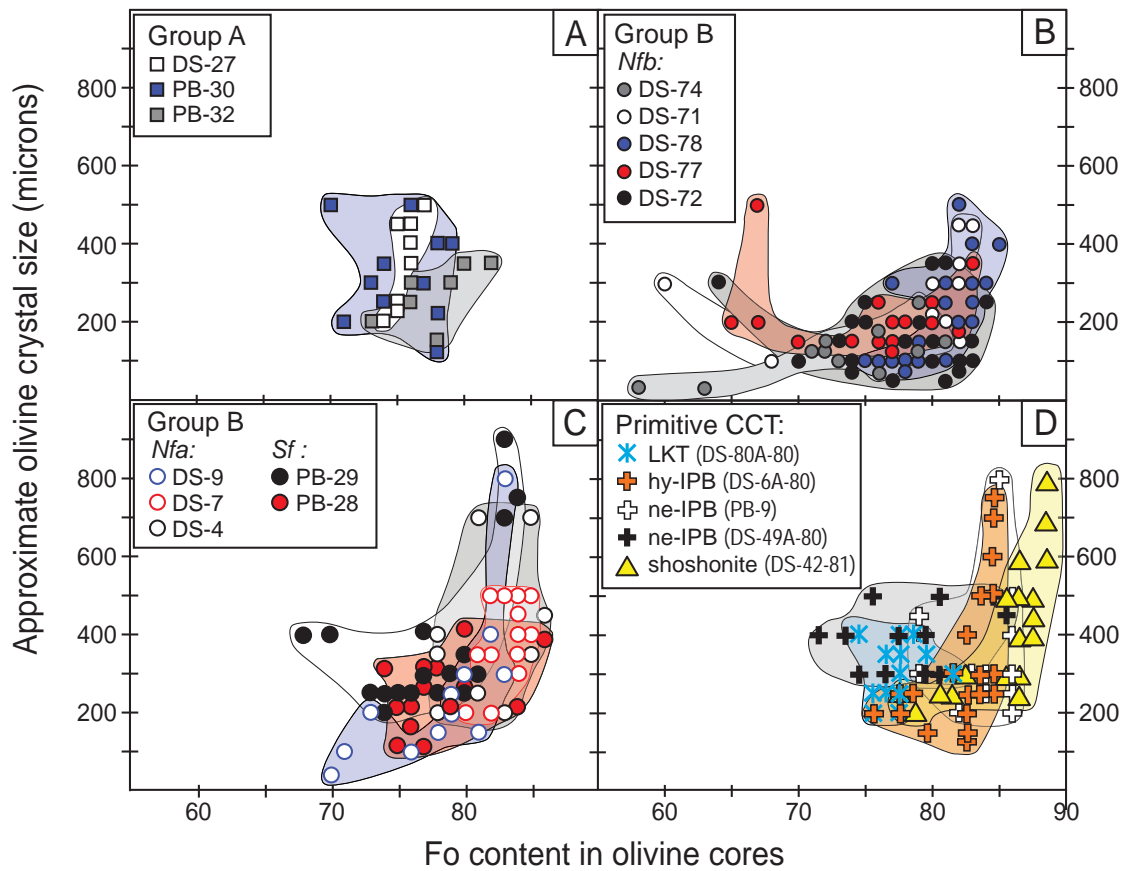
Figure 6.
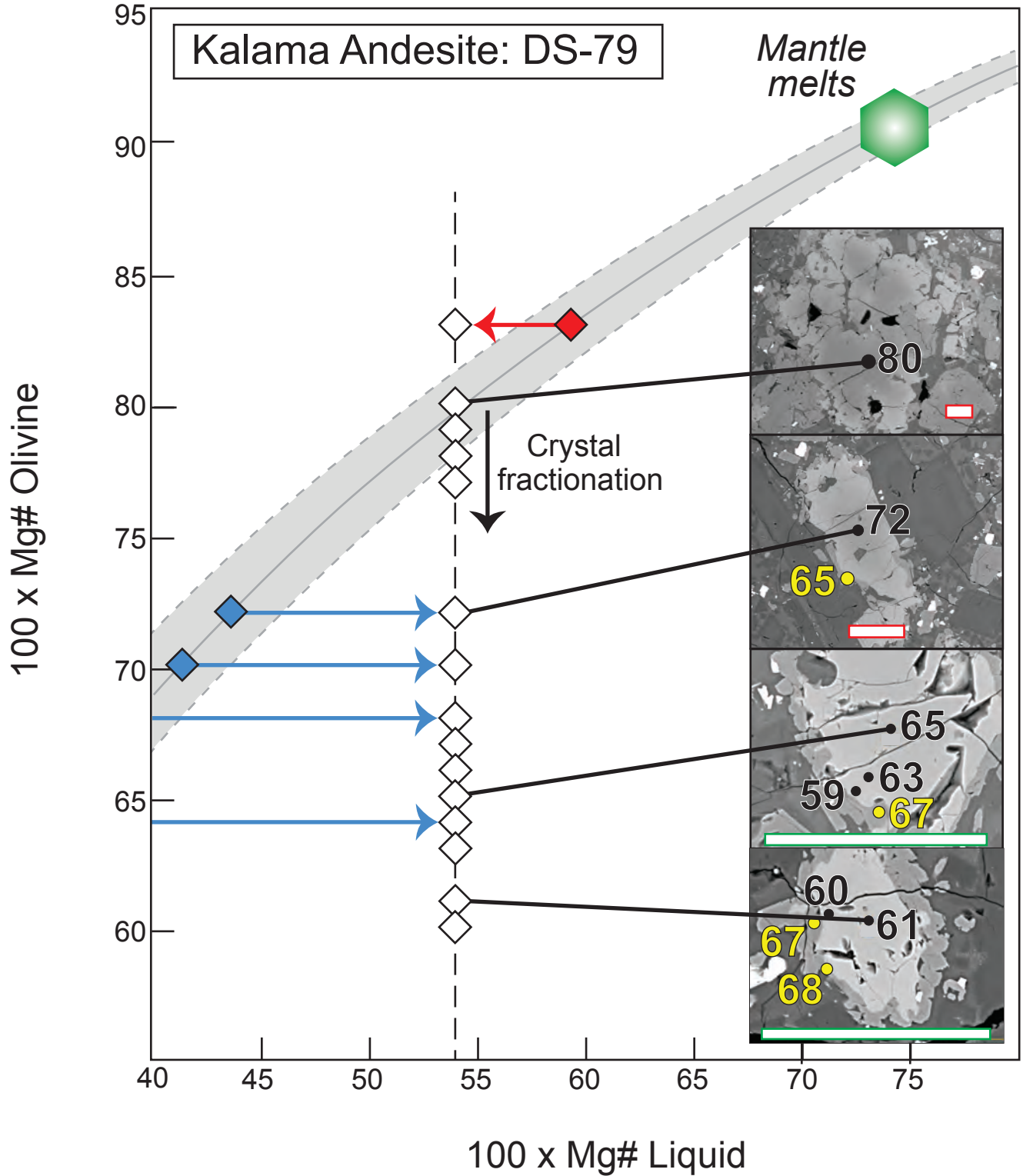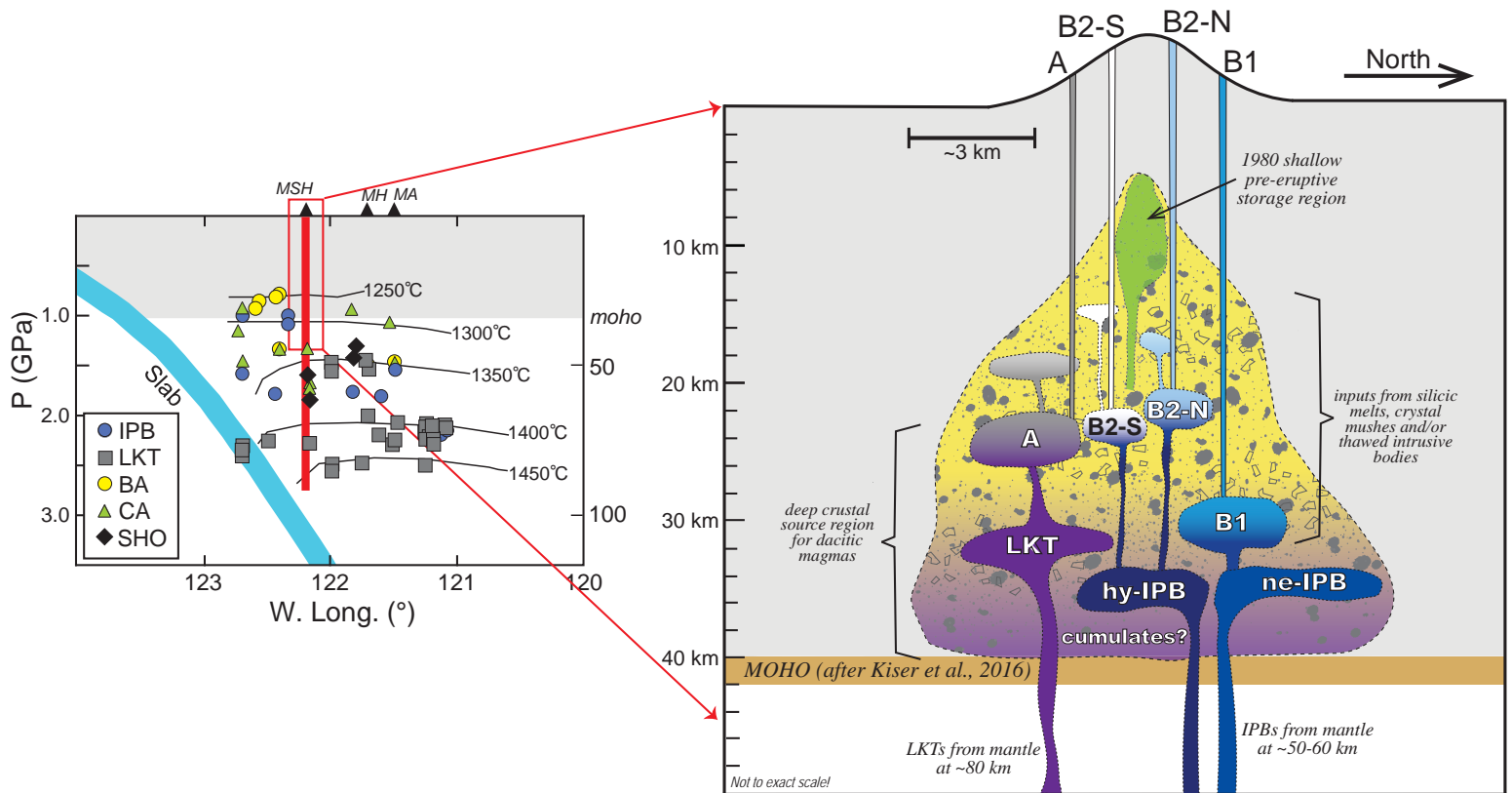
FIGURE 7
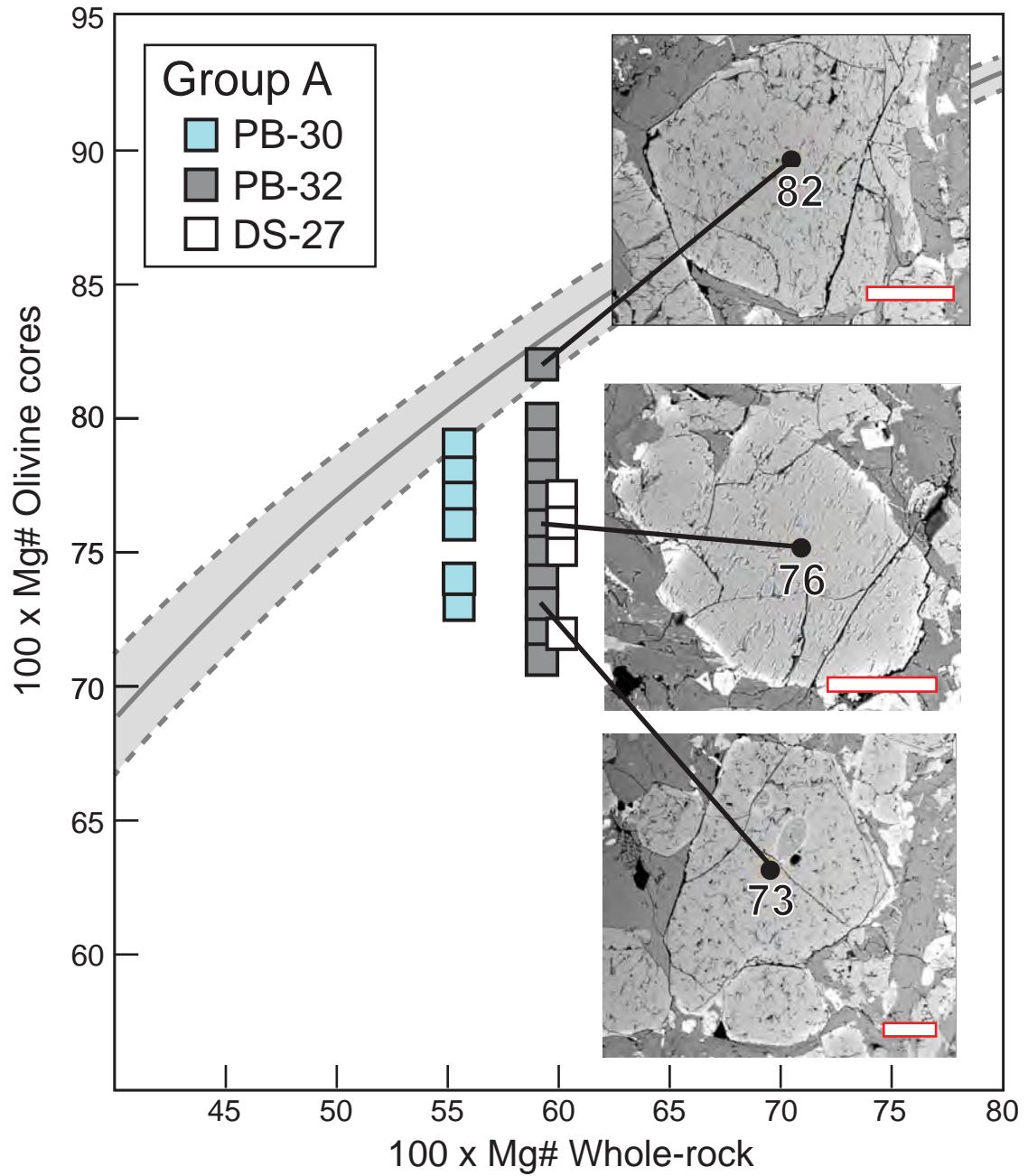
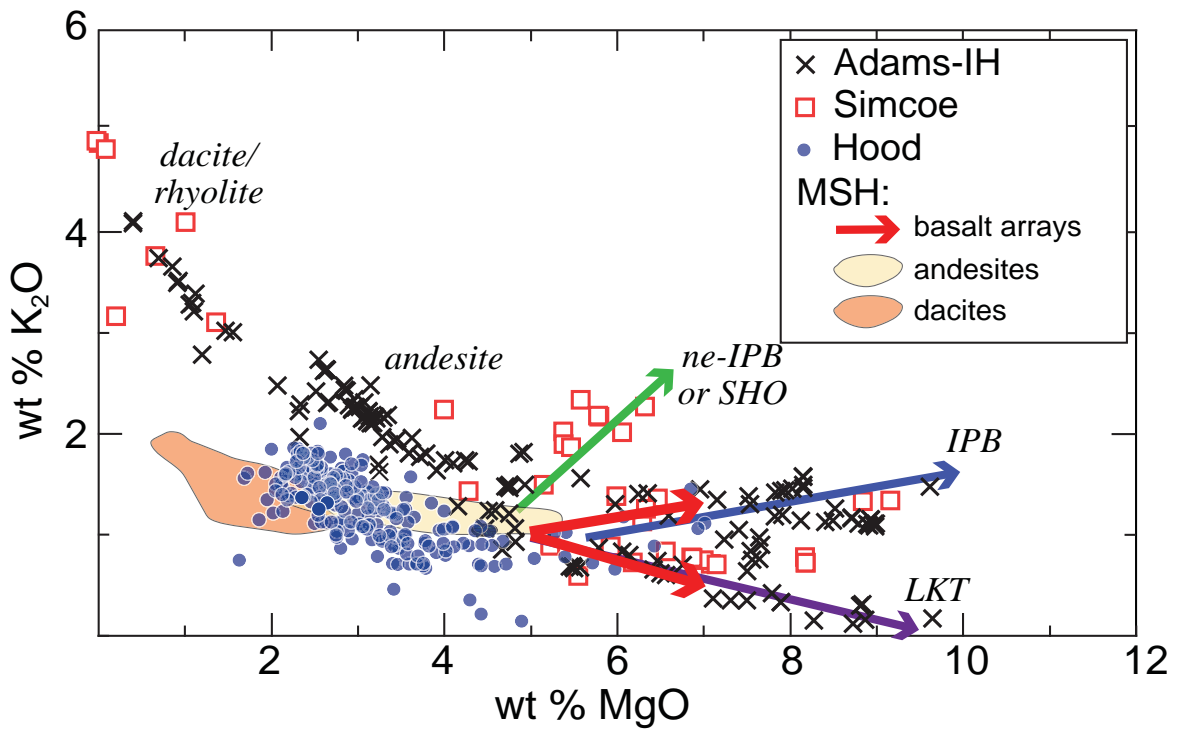# Figure 8
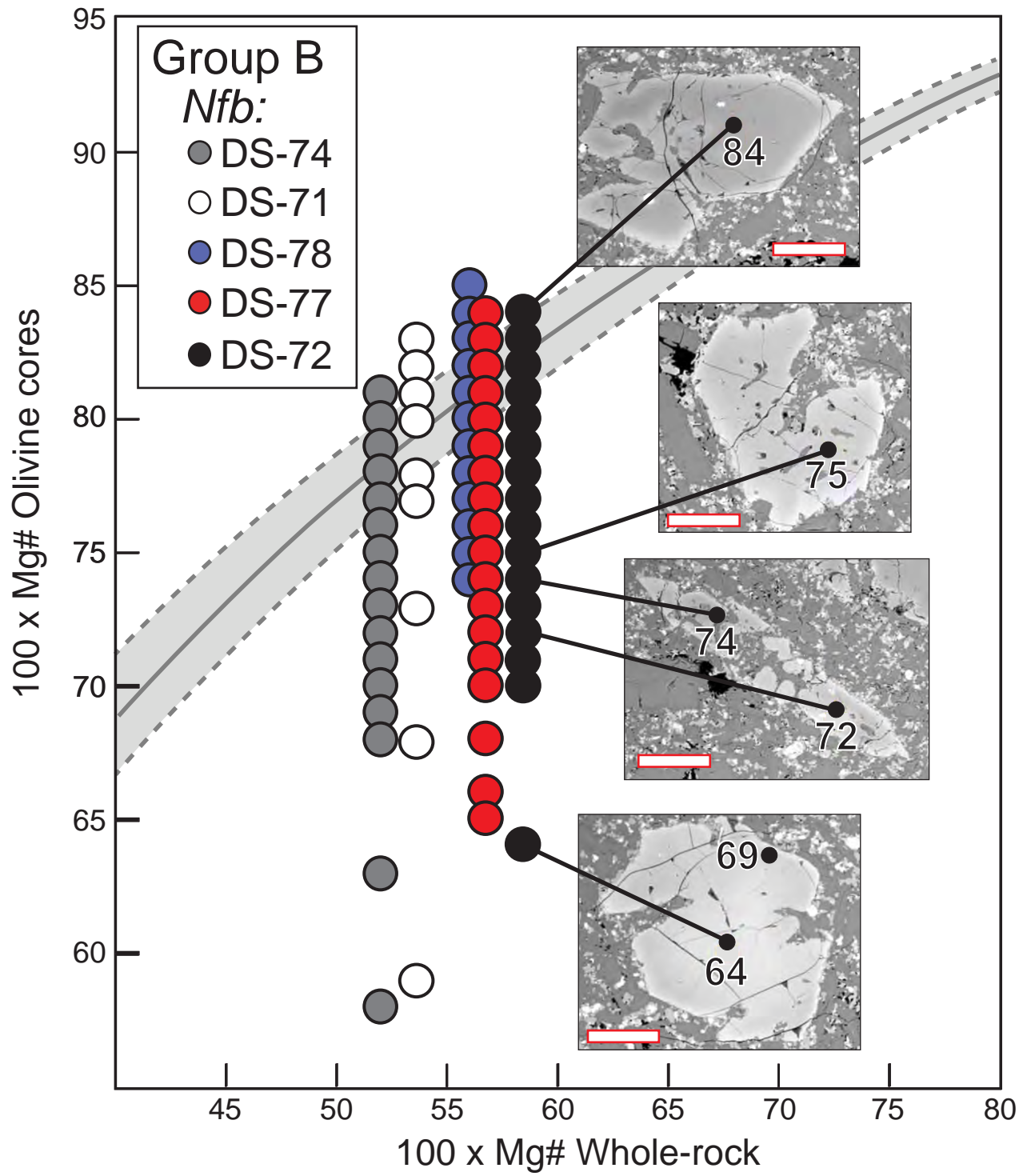
Figure 9
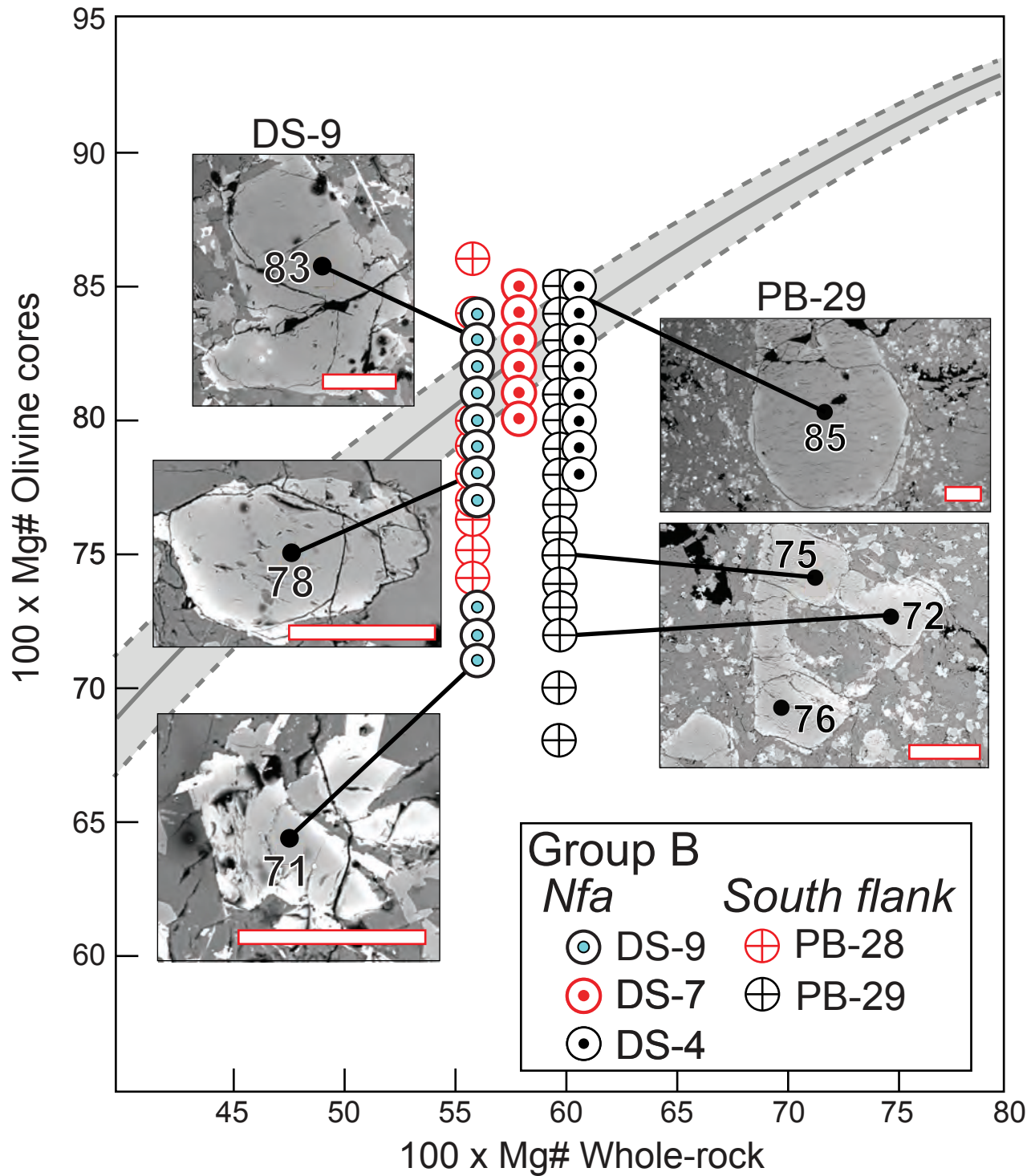
FIGURE 10
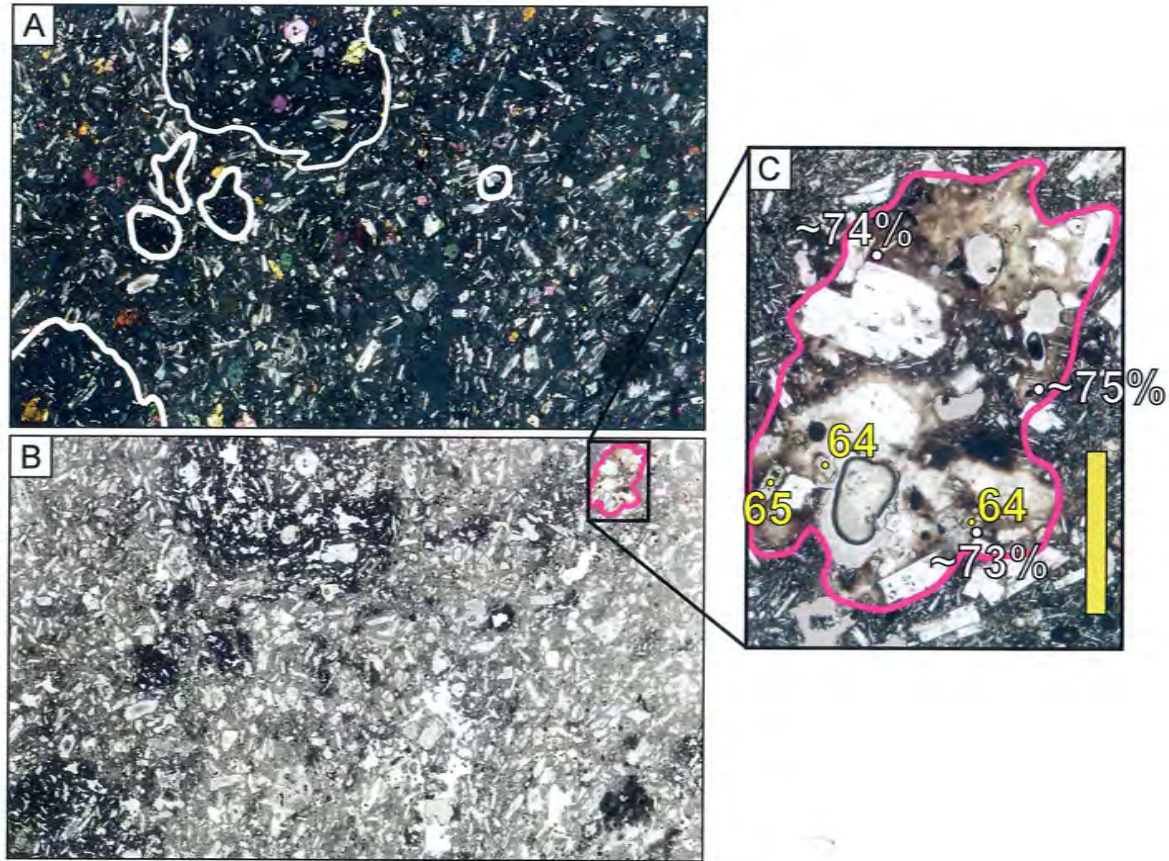
Figure 11
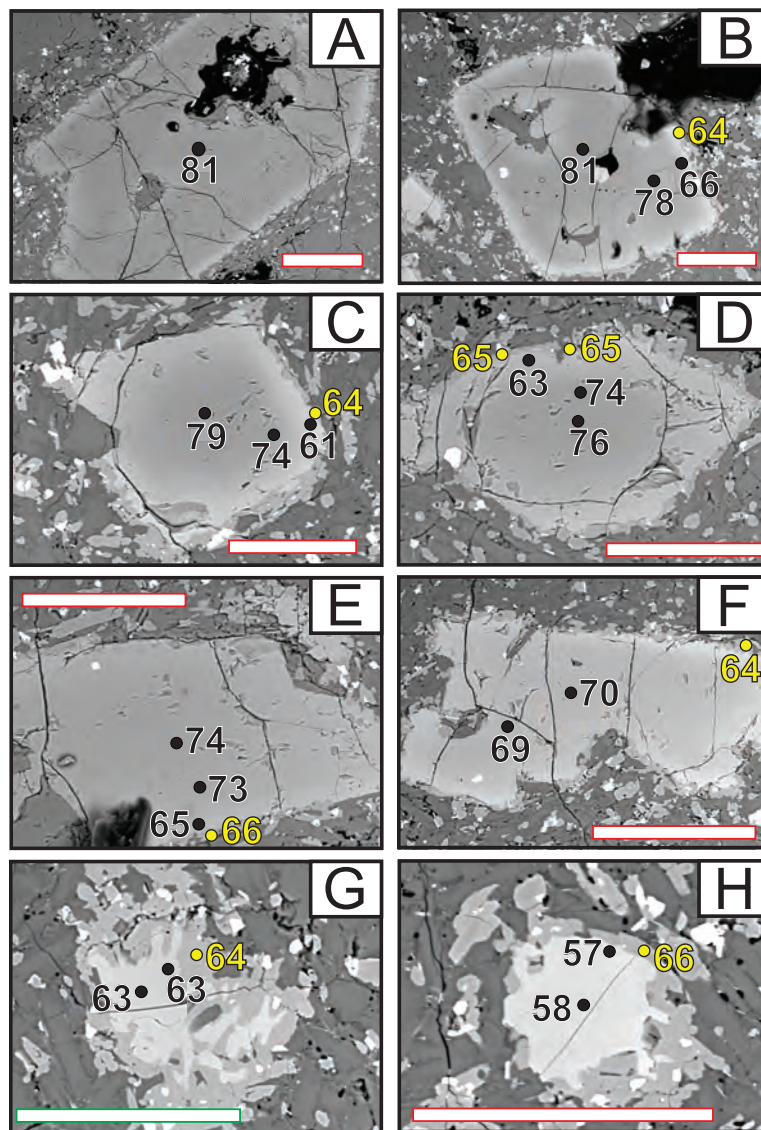
Figure 12

FIGURE 13

Figure 14

Figure 15

Figure 16